GLOBAL-SCALE TURBULENT CONVECTION AND MAGNETIC DYNAMO ACTION IN THE SOLAR ENVELOPE

ALLAN SACHA BRUN

DSM/DAPNIA/SAp, CEA Saclay, 91191 Gif-sur-Yvette Cedex, France

MARK S. MIESCH

High Altitude Observatory, National Center for Atmospheric Research, Boulder, CO 80307-3000

AND

JURI TOOMRE

JILA, University of Colorado, 440 UCB, Boulder, CO 80309-0440

ABSTRACT

The operation of the solar global dynamo appears to involve many dynamical elements, including the generation of fields by the intense turbulence of the deep convection zone, the transport of these fields into the tachocline region near the base of the convection zone, the storage and amplification of toroidal fields in the tachocline by differential rotation, and the destabilization and emergence of such fields due to magnetic buoyancy. Self-consistent magnetohydrodynamic (MHD) simulations that realistically incorporate all of these processes are not yet computationally feasible, although some elements can now be studied with reasonable fidelity. Here we consider the manner in which turbulent compressible convection within the bulk of the solar convection zone can generate large-scale magnetic fields through dynamo action. We accomplish this through a series of three-dimensional numerical simulations of MHD convection within rotating spherical shells using our anelastic spherical harmonic (ASH) code on massively parallel supercomputers. Since differential rotation is a key ingredient in all dynamo models, we also examine here the nature of the rotation profiles that can be sustained within the deep convection zone as strong magnetic fields are built and maintained. We find that the convection is able to maintain a solar-like angular velocity profile despite the influence of Maxwell stresses, which tend to oppose Reynolds stresses and thus reduce the latitudinal angular velocity contrast throughout the convection zone. The dynamo-generated magnetic fields exhibit a complex structure and evolution, with radial fields concentrated in downflow lanes and toroidal fields organized into twisted ribbons that are extended in longitude and achieve field strengths of up to 5000 G. The flows and fields exhibit substantial kinetic and magnetic helicity although systematic hemispherical patterns are only apparent in the former. Fluctuating fields dominate the magnetic energy and account for most of the back-reaction on the flow via Lorentz forces. Mean fields are relatively weak and do not exhibit systematic latitudinal propagation or periodic polarity reversals as in the Sun. This may be attributed to the absence of a tachocline, i.e., a penetrative boundary layer between the convection zone and the deeper radiative interior possessing strong rotational shear. The influence of such a layer will await subsequent studies.

Subject headings: convection — MHD — Sun: magnetic fields — turbulence

1. TURBULENT MAGNETIC SUN

The Sun is a magnetic star whose variable activity has profound effects on our technological society on Earth. The high-speed solar wind and its energetic particles, coronal mass ejections, and explosive flares are all linked to the changing magnetic fields within the extended solar atmosphere. Such events can serve to damage satellites in space and power grids on the ground and interrupt communications. Thus, there is keen interest in being able to forecast the behavior of the magnetic structures. Yet this has proved to be difficult, since the eruption of new magnetic flux through the solar surface appears to have a dominant role in the evolution of field configurations in the solar atmosphere, as does the shuffling of field footpoints by the subsurface turbulence.

The origin of the solar magnetic fields must rest with dynamo processes occurring deep within the star in the spherical shell of intensely turbulent convection that occupies the outer 29% in radius below the solar surface. Within this convection zone, complex interactions between compressible turbulence

and rotation of the star serve to redistribute angular momentum so that a strong differential rotation is achieved. Further, since the fluid is electrically conducting, currents will flow and magnetic fields must be built. However, there are many fundamental puzzles about the dynamo action that yields the observed fields.

The magnetic fields, like the underlying turbulence, can be both orderly on some scales and chaotic on others. Most striking is that the Sun exhibits 22 yr cycles of global magnetic activity, involving sunspot eruptions with very well defined rules for field parity and emergence latitudes as the cycle evolves. Coexisting with these large-scale ordered magnetic structures are small-scale but intense magnetic fluctuations that emerge over much of the solar surface, with little regard for the solar cycle. This diverse range of activity is most likely generated by two conceptually distinct magnetic dynamos (e.g., Weiss 1994; Childress & Gilbert 1995; Cattaneo 1999; Cattaneo & Hughes 2001; Ossendrijver 2003). These involve a *small-scale dynamo*, functioning within the intense turbulence of the upper convection zone, that builds the chaotic magnetic

fluctuations and a *global dynamo*, operating within both the deeper convection zone and the strong rotational shear of the tachocline at its base, that builds the more ordered fields.

1.1. *Building Magnetic Fields in the Sun*

The pairing of opposite-polarity sunspots in the east-west direction within active regions is most readily interpreted as the surface emergence of large-scale toroidal field structures. These structures are created somewhere below the photosphere and rise upward, bending to pierce the photosphere in the form of curved tubes. The current paradigm for large-scale dynamo action (e.g., Parker 1993) involves two major components. First, strong toroidal field structures must be generated. This is believed to occur as a result of the stretching that any differential rotation in latitude or radius will impose on any weak existing poloidal field. This first process is often referred to as the ω-effect after its parameterization within the framework of mean field electrodynamics (e.g., Moffatt 1978; Krause & Rädler 1980; Parker 1989). Helioseismology has shown that gradients in angular velocity are particularly strong in the tachocline, pointing to this interface region between the convection zone and the deeper radiative interior as the likely site for the generation of strong toroidal fields. Second, an inverse process is required to complete the cycle, regenerating the poloidal field from the toroidal field. Different theories exist for the operation of this process (known as the α-effect). Some have the poloidal field regenerated at the surface through the breakup and reconnection of the large-scale field that emerges as active regions, where this field has gained a poloidal component owing to Coriolis forces during its rise, with meridional flows having a key role in transporting such flux both poleward and down toward the tachocline (e.g., Babcock 1961; Leighton 1969; Wang & Sheeley 1991; Durney 1997; Dikpati & Charbonneau 1999). Others believe that the poloidal field is regenerated by the cumulative action of many small-scale cyclonic turbulent motions on the field throughout the convection zone, rather than just close to the surface (e.g., Parker 1993). In either scenario, there is separation in the sites of generation of toroidal field (in the strong shear of the tachocline) and regeneration of poloidal field (either near the surface or in the bulk of the convection zone), yielding what is now broadly called an *interface dynamo* (Parker 1993). Recent mean field dynamo approaches (e.g., Rüdiger & Brandenburg 1995; Tobias 1996; Charbonneau & MacGregor 1997; Beer et al. 1998) suggest that such an interface model can circumvent the problem of strong α-quenching by mean magnetic fields (Cattaneo & Hughes 1996), thereby being capable of yielding field strengths comparable to those inferred from observations.

The interface dynamo paradigm is thus based on the following underlying processes or building blocks:

1. The α-effect: the generation of the background weak poloidal field, either by cyclonic turbulence within the convection zone or by breakup of active regions.

2. The β-effect or turbulent transport: the transport of the weak poloidal field from its generating region to the region of strong shear, the tachocline.

3. The ω-effect: the organization and amplification of the magnetic field by differential rotation, particularly by large-scale rotational shear in the tachocline, into strong, isolated magnetic structures that are toroidal in character.

4. Magnetic buoyancy: the rise and transport of the large-scale toroidal field by magnetic buoyancy into and through the convection zone either to be shredded and recycled or to emerge as active regions.

Since all models presume close linkages between the differential rotation of the Sun and the operation of its global dynamo, let us briefly review what is known about the angular velocity Ω profile with radius and latitude. Helioseismology, which involves the study of the acoustic p-mode oscillations of the solar interior (e.g., Gough & Toomre 1991), has provided a new window for studying dynamical processes deep within the Sun. This has been enabled by the nearly continuous and complementary helioseismic observations provided from the vantage point of both the *SOHO* spacecraft with the high-resolution Michelson Doppler Imager (SOI MDI; Scherrer et al. 1995) and the ground-based Global Oscillation Network Group (GONG) set of six related instruments distributed at different longitudes across the Earth (Harvey et al. 1996). Helioseismology has revealed that the rotation profiles obtained by inversion of frequency splittings of the p-modes (e.g., Thompson et al. 1996, 2003; Schou et al. 1998; Howe et al. 2000) have a striking behavior that is unlike any anticipated by convection theory prior to such probing of the interior of a star. The strong latitudinal variation of angular velocity Ω observed near the surface, where the rotation is considerably faster at the equator than near the poles, extends through much of the convection zone depth (about 200 Mm) with relatively little radial dependence. Another striking feature is the tachocline (e.g., Spiegel & Zahn 1992), a region of strong shear at the base of the convection zone where Ω adjusts to apparent solid-body rotation in the deeper radiative interior. A thin *near-surface shear layer* is also present in which Ω increases with depth at intermediate and low latitudes. This subsurface region is now being intensively probed using local domain helioseismic methods, revealing the presence of remarkable large-scale meandering flow fields much like jet streams, banded zonal flows, and evolving meridional circulations, all of which contribute to what is called solar subsurface weather (SSW; Haber et al. 2000, 2002; Toomre 2002).

1.2. *Studying Elements of the Global Dynamo*

Computational resources are currently insufficient to enable modeling a complete dynamical system incorporating all the diverse aspects of the large-scale solar dynamo. Our goal is therefore to study individually some of the essential processes, with a view to eventually combine such findings into a more complete nonlinear interface-type solar dynamo model as resources become available. In this spirit, there has been substantial theoretical progress recently in trying to understand how the differential rotation profiles deduced from helioseismology may be established in the bulk of the convection zone. Building on the early three-dimensional numerical simulations of rotating convection in spherical shells (e.g., Gilman & Miller 1981; Glatzmaier & Gilman 1982; Glatzmaier 1985a, 1985b, 1987; Sun & Schubert 1995), recent modeling using the anelastic spherical harmonic (ASH) code on massively parallel supercomputers (e.g., Miesch et al. 2000; Elliott et al. 2000; Brun & Toomre 2002) has permitted attaining fairly turbulent states of convection in which the resulting Ω profiles now begin to capture many elements of the deduced interior profiles. These simulations possess fast equatorial rotation, substantial contrasts in Ω with latitude, and reduced tendencies for Ω to be constant on cylinders. The role of the Reynolds stresses and of meridional circulations within such convection in redistributing the angular momentum to achieve such

differential rotation over much of the convection zone is becoming evident. However, the simulations with ASH have only just begun to examine how the near-surface rotational shear layer may be established (DeRosa et al. 2002), whereas the formation and maintenance of a tachocline near the base of the convection zone have only been tentatively considered within three-dimensional simulations that admit downward penetration (Miesch et al. 2000).

Dynamics within the solar tachocline and overshoot region are thought to be extremely complex (e.g., Gilman 2000; Ossendrijver 2003). The upper portion of the tachocline may extend into the convective envelope, whereas the lower portion consists of a stably stratified, magnetized shear flow. Turbulent penetrative convection transfers mass, momentum, energy, and magnetic fields between the convection zone and radiative interior both directly and through the generation of internal waves, particularly gravity waves, which can drive oscillatory zonal flows and large-scale circulations. Instabilities driven by shear and magnetic buoyancy further influence the structure and evolution of the tachocline and likely play an important role in the solar activity cycle. Understanding these various processes will require much future work beyond the scope of this paper.

Our objective here is to expand on the purely hydrodynamical simulations with ASH to begin to study the magnetic dynamo action that can be achieved by global-scale turbulent flows within the bulk of the solar convection zone. These studies build on the pioneering modeling that was able to resolve fairly laminar but intricate magnetohydrodynamic (MHD) convection and its dynamo action within rotating spherical shells (e.g., Gilman & Miller 1981; Gilman 1983; Glatzmaier 1987). Other related dynamo simulations have also considered deeper shells (e.g., Kageyama et al. 1993; Kageyama & Sato 1997). We turn now to more complex states associated with the turbulent flows that can be resolved using the ASH code. Much as in Brun & Toomre (2002) and its immediate progenitors, we deal primarily with the bulk of the convection zone by imposing stress-free and impenetrable upper and lower boundaries to the shell, thereby ignoring the region of penetration of flows into the deeper radiative interior. Thus, issues concerning the tachocline are not dealt with, including the downward transport of magnetic fields (β-effect) into this region where strong toroidal fields may be stretched into existence. Likewise the stability of these fields and the buoyant rise and emergence of flux tubes are not studied in detail, although magnetic buoyancy is allowed in our ASH simulations via the anelastic approximation. Rather, the simulations reported here examine the α- and ω-effects within much of the convective interior, inspired particularly by the Gilman & Miller (1981) studies, but now having the ability to resolve turbulent convection and the fairly realistic differential rotation that it is able to sustain.

The convection in many previous studies of dynamo action in rotating spherical shells is dominated by so-called banana cells: columnar rolls aligned with the rotation axis. These cells possess substantial helicity and generally drive a large differential rotation, thus providing all the necessary ingredients for an α-ω dynamo. Sustained dynamo action is indeed observed for a variety of parameter regimes, but the results are generally not solar-like. The first studies by Gilman & Miller (1981) revealed no solutions with periodic field reversals. Cyclic, dipolar dynamos were found by Gilman (1983) and Glatzmaier (1984, 1985a, 1985b) for somewhat higher Rayleigh numbers, but the periods were significantly shorter than the solar

activity cycle ($\sim$1–10 yr) and toroidal fields were found to propagate poleward during the course of a cycle rather than equatorward as in the Sun. Furthermore, these relatively low resolution simulations could not capture the intricate structure of the fluctuating field components known to exist in the solar atmosphere.

More recent simulations of MHD convection in rotating spherical shells have generally focused on parameter regimes more characteristic of the geodynamo and other planetary interiors (e.g., Kageyama & Sato 1997; Christensen et al. 1999; Roberts & Glatzmaier 2000; Busse 2000a, 2000b; Ishihara & Kida 2002). Relative to the Sun, convective motions in the planetary interiors are much more influenced by rotation (lower Rossby numbers) and diffusion (lower Reynolds and magnetic Reynolds numbers) and much less influenced by compressibility (mild density stratification). Although such simulations have achieved higher resolution relative to Gilman and Glatzmaier's earlier work, they are still generally dominated by banana cells owing to the strong rotational influence. They often tend to produce mean fields of a dipolar nature, although quadrupolar configurations are preferred in some parameter regimes, generally characterized by high Rayleigh numbers and low magnetic Prandtl numbers (Grote et al. 1999, 2000; Busse 2000b). Cyclic solutions have been found, but field reversals are more often aperiodic, particularly for high Rayleigh numbers.

In this paper we report simulations of hydromagnetic dynamo action in the solar convection zone at unprecedented spatial resolution. Our primary objective is to gain a better understanding of magnetic field amplification and transport by turbulent convection in the solar envelope and the essential role that such processes play in the operation of the solar dynamo. In § 2 we describe our numerical model and our simulation strategy in which we introduce a small seed magnetic field into an existing hydrodynamic simulation. In § 3 we discuss some properties of this hydrodynamic progenitor simulation and the exponential growth and nonlinear saturation of the seed field. We then investigate the intricate structure and evolution of the dynamo-generated fields in § 4 and their back-reaction on mean flows in § 5. Here we focus on the turbulent or fluctuating (nonaxisymmetric) field components that are found to dominate the magnetic energy. We consider the mean (axisymmetric) field components separately in § 6. In § 7 we discuss the magnetic and kinetic helicity found in our dynamo simulations and present spectra and probability density functions (pdf's) for various fields. We summarize our primary results and conclusions in § 8.

2. MODELING APPROACH

2.1. *Anelastic MHD Equations*

In this paper we report three-dimensional numerical experiments designed to investigate the complex MHD of the solar convection zone in spherical geometries. We have extended our already well-tested hydrodynamic ASH code (see Clune et al. 1999; Miesch et al. 2000; Brun & Toomre 2002) to include the magnetic induction equation and the feedback of the field on the flow via Lorentz forces and ohmic heating. Thus, the ASH code is now able to solve the full set of three-dimensional MHD anelastic equations of motion in a rotating, convective spherical shell (Glatzmaier 1984) with high resolution on massively parallel computing architectures. These equations are fully nonlinear in velocity and magnetic field variables, but under the anelastic approximation the thermodynamic variables are linearized with respect to a

spherically symmetric and evolving mean state having a density $\bar{\rho}$, pressure $\bar{P}$, temperature $\bar{T}$, and specific entropy $\bar{S}$. Fluctuations about this mean state are denoted by ρ, P, T, and S. The resulting equations are

$$\nabla \cdot (\bar{\rho}\boldsymbol{v}) = 0, \tag{1}$$

$$\nabla \cdot \boldsymbol{B} = 0, \tag{2}$$

$$\bar{\rho}\left[\frac{\partial \boldsymbol{v}}{\partial t} + (\boldsymbol{v}\cdot\nabla)\boldsymbol{v} + 2\Omega_0 \times \boldsymbol{v}\right] = -\nabla P + \rho g + \frac{1}{4\pi}(\nabla \times \boldsymbol{B}) \times \boldsymbol{B}$$
$$- \nabla \cdot \boldsymbol{\mathcal{D}} - (\nabla \bar{P} - \bar{\rho} g), \tag{3}$$

$$\bar{\rho}\bar{T}\frac{\partial S}{\partial t} + \bar{\rho}\bar{T}\boldsymbol{v}\cdot\nabla(\bar{S}+S) = \nabla \cdot [\kappa_r \bar{\rho} c_p \nabla(\bar{T}+T)$$
$$+ \kappa \bar{\rho}\bar{T}\nabla(\bar{S}+S)] + \frac{4\pi\eta}{c^2}\boldsymbol{j}^2 + 2\bar{\rho}\nu\left[e_{ij}e_{ij} - \frac{1}{3}(\nabla\cdot\boldsymbol{v})^2\right] + \bar{\rho}\epsilon, \tag{4}$$

$$\frac{\partial \boldsymbol{B}}{\partial t} = \nabla \times (\boldsymbol{v} \times \boldsymbol{B}) - \nabla \times (\eta \nabla \times \boldsymbol{B}), \tag{5}$$

where $\boldsymbol{v} = (v_r, v_\theta, v_\phi)$ is the local velocity in spherical coordinates in the frame rotating at constant angular velocity Ω_0, $\boldsymbol{g}$ is the gravitational acceleration, $\boldsymbol{B} = (B_r, B_\theta, B_\phi)$ is the magnetic field, $\boldsymbol{j} = (c/4\pi)(\nabla \times \boldsymbol{B})$ is the current density, c_p is the specific heat at constant pressure, κ_r is the radiative diffusivity, η is the effective magnetic diffusivity, and $\boldsymbol{\mathcal{D}}$ is the viscous stress tensor, involving the components

$$\mathcal{D}_{ij} = -2\bar{\rho}\nu\left[e_{ij} - \tfrac{1}{3}(\nabla\cdot\boldsymbol{v})\delta_{ij}\right], \tag{6}$$

where e_{ij} is the strain rate tensor and ν and κ are effective eddy diffusivities. A volume heating term $\bar{\rho}\epsilon$ is also included in these equations for completeness, but it is insignificant in the solar envelope. When our model is applied to other stars, such as A-type stars (Browning et al. 2004), this term represents energy generation by nuclear burning. To complete the set of equations, we use the linearized equation of state

$$\frac{\rho}{\bar{\rho}} = \frac{P}{\bar{P}} - \frac{T}{\bar{T}} = \frac{P}{\gamma\bar{P}} - \frac{S}{c_p}, \tag{7}$$

where γ is the adiabatic exponent, and assume the ideal gas law

$$\bar{P} = \mathcal{R}\bar{\rho}\bar{T}, \tag{8}$$

where $\mathcal{R}$ is the gas constant. The reference or mean state (indicated by overbars) is derived from a one-dimensional solar structure model (Brun et al. 2002) and is continuously updated with the spherically symmetric components of the thermodynamic fluctuations as the simulation proceeds. It begins in hydrostatic balance so the bracketed term on the right-hand side of equation (3) initially vanishes. However, as the simulation evolves, turbulent and magnetic pressure drives the reference state slightly away from hydrostatic balance.

Because of limitations in computing resources, no simulation achievable now or in the near future can hope to directly capture all scales of solar convection from global to molecular dissipation scales. The simulations reported here resolve nonlinear interactions among a larger range of scales than any previous MHD model of global-scale solar convection, but motions still must exist in the Sun on scales smaller than our grid resolution. In this sense, our models should be regarded as large-eddy simulations (LESs) with parameterizations to account for subgrid-scale (SGS) motions. Thus, the effective eddy diffusivities ν, κ, and η represent momentum, heat, and magnetic field transport by motions that are not resolved by the simulation. They are allowed to vary with radius but are independent of latitude, longitude, and time for a given simulation. Their amplitudes and radial profiles are varied depending on the resolution and objectives of each simulation. In the simulations reported here, ν, κ, and η are assumed to be proportional to $\bar{\rho}^{-1/2}$.

The velocity, magnetic, and thermodynamic variables are expanded in spherical harmonics $Y_{\ell m}(\theta, \phi)$ for their horizontal structure and in Chebyshev polynomials $T_n(r)$ for their radial structure (see the Appendix). This approach has the advantage that the spatial resolution is uniform everywhere on a sphere when a complete set of spherical harmonics is used up to some maximum in degree ℓ (retaining all azimuthal orders $m \leq \ell$ in what is known as triangular truncation).

The anelastic approximation captures the effects of density stratification without having to resolve sound waves, which would severely limit the time step. In the MHD context, the anelastic approximation filters out fast magnetoacoustic waves but retains the Alfvén and slow magnetoacoustic modes. In order to ensure that the mass flux and the magnetic field remain divergenceless to machine precision throughout the simulation, we use a toroidal-poloidal decomposition as

$$\bar{\rho}\boldsymbol{v} = \nabla \times \nabla \times (W\hat{\boldsymbol{e}}_r) + \nabla \times (Z\hat{\boldsymbol{e}}_r), \tag{9}$$

$$\boldsymbol{B} = \nabla \times \nabla \times (C\hat{\boldsymbol{e}}_r) + \nabla \times (A\hat{\boldsymbol{e}}_r). \tag{10}$$

The Appendix lists the full set of anelastic MHD equations as solved by the numerical algorithm, involving the spherical harmonic coefficients of the stream functions W and Z and the magnetic potentials C and A. This system of equations requires 12 boundary conditions in order to be well posed. Since assessing the angular momentum redistribution in our simulations is one of the main goals of this work, we have opted for torque-free velocity and magnetic boundary conditions:

1. Impenetrable top and bottom: $v_r = 0|_{r=r_{\rm bot}, r_{\rm top}}$.
2. Stress-free top and bottom: $(\partial/\partial r)(v_\theta/r) = (\partial/\partial r)(v_\phi/r) = 0|_{r=r_{\rm bot}, r_{\rm top}}$.
3. Constant entropy gradient at top and bottom: $\partial\bar{S}/\partial r = {\rm const}|_{r=r_{\rm bot}, r_{\rm top}}$.
4. Match to an external potential magnetic field at top and bottom: $\boldsymbol{B} = \nabla\Phi \Rightarrow \Delta\Phi = 0|_{r=r_{\rm bot}, r_{\rm top}}$, or impose a purely radial magnetic field at top and bottom (match to highly permeable external media; Jackson 1999), i.e., $B_\theta = B_\phi = 0|_{r=r_{\rm bot}, r_{\rm top}}$.

The main difference between having a potential or a purely radial magnetic field is that with the latter the Poynting flux is zero at the shell surface, and thus there is no leakage of magnetic energy through the boundaries (see § 3.2).

2.2. Numerical Experiments

Our numerical model is a simplified portrayal of the solar convection zone: solar values are taken for the heat flux, rotation rate, mass, and radius, and a perfect gas is assumed. The computational domain extends from $0.72R_*$ to $0.97R_*$ (with R_* the solar radius), thereby focusing on the bulk of the unstable zone without yet considering penetration into the radiative interior or smaller scale convective motions near the photosphere. The depth of the convection zone is therefore

TABLE 1
Parameters for the Four Simulations

Parameter	H	M1	M2	M3
N_r, N_θ, N_ϕ	64, 256, 512	64, 256, 512	64, 256, 512	128, 512, 1024
Ra	8.1×10^4	8.1×10^4	8.1×10^4	8.1×10^4
Pr_m	. . .	2	2.5	4
Ro_c	0.73	0.73	0.73	0.73
η (cm^2 s^{-1})	. . .	7×10^{11}	5.6×10^{11}	3.5×10^{11}
τ_η (days)	. . .	495	620	990
Re	136	136	133	121
Re_m	. . .	272	334	486
Λ	. . .	1.5×10^{-3}	4.5×10^{-2}	20
Pe	20	17	16	15
Ro	0.15	0.12	0.12	0.11

Notes.—N_r, N_θ, and N_ϕ are the number of radial, latitudinal, and longitudinal mesh points, respectively. All simulations have an inner radius $r_{bot} = 5.0 \times 10^{10}$ cm and an outer radius $r_{top} = 6.72 \times 10^{10}$ cm, and all quantities listed here are evaluated at midlayer depth. In all cases, $\nu = 1.4 \times 10^{12}$ and $\kappa = 1.1 \times 10^{13}$ at midlayer depth and the Prandtl number Pr $= \nu/\kappa = 0.125$. Furthermore, the rotation rate of the coordinate system $\Omega_0 = 2.6 \times 10^{-6}$ s^{-1} in all cases, yielding a Taylor number of Ta $= 4\Omega_0^2 L^4/\nu^2 = 1.2 \times 10^6$, where $L = r_{top} - r_{bot}$. Also listed are the Rayleigh number Ra $= (-\partial\bar{\rho}/\partial S)\Delta SgL^3/\rho\nu\kappa$, the magnetic Prandtl number $Pr_m = \nu/\eta$, the convective Rossby number $Ro_c = (Ra/Ta\,Pr)^{1/2}$, the Reynolds number Re $= \tilde{v}'L/\nu$, the magnetic Reynolds number $Re_m = \tilde{v}'L/\eta$, the Elssasser number $\Lambda = \tilde{B}^2/4\pi\bar{\rho}\eta\Omega_0$, the Péclet number Pe $= Re\,Pr = \tilde{v}'L/\kappa$, the Rossby number Ro $= \tilde{v}'/2\Omega_0 L$, and the ohmic diffusion time $\tau_\eta = L^2/(\pi^2\eta)$, where $\tilde{v}'$ is the rms convective velocity and $\tilde{B}$ is the rms magnetic field. A Reynolds number based on the peak velocity at midlayer depth would be about a factor of 5 larger.

$L = 1.72 \times 10^{10}$ cm, and the background density varies across the shell by about a factor of 30. Outward heat transport by unresolved convective motions near the surface is modeled by locally increasing the component of the SGS eddy diffusivity κ, which operates on the mean (horizontally averaged) entropy gradient, thus allowing the simulation to achieve flux equilibrium (see § 3.2). Meanwhile, the influence of unresolved motions on the flow itself is taken into account through the SGS eddy diffusivities ν, κ, and η.

The magnetic simulations discussed here were all initiated from the same nonmagnetic progenitor simulation, which we refer to as case H. Case H is well evolved, with a complex convective structure and a solar-like differential rotation profile (§ 3.1).

A small seed magnetic field is then introduced and its evolution is followed via the induction equation. The seed field is dipole in nature but soon develops a more complicated structure as it is amplified by the convective motions. If the magnetic diffusivity is sufficiently small, the field will continue to amplify until it reaches a nonlinear saturation level where production balances dissipation. In order to determine whether sustained dynamo action is achieved, the simulation must be evolved for at least several ohmic diffusion times $\tau_\eta = L^2/(\pi^2\eta)$ (see Moffatt 1978; Jacobs 1987). We have conducted three MHD simulations, cases M1, M2, and M3, each with progressively lower values of the magnetic diffusivity (see Table 1).

It is currently impractical to perform dynamo calculations with a spatial resolution comparable to our most turbulent hydrodynamic cases ($N_\theta = 1024$, $N_\phi = 2048$, $N_r = 256$), which achieve a rms Reynolds number Re of over 700. The increased workload required to solve the magnetic induction equation and the long time integrations necessary to reliably assess dynamo action cannot be easily achieved with currently available computational resources. In order to achieve dynamo action in more moderately turbulent simulations such as those considered here (Re ~ 150), the magnetic Prandtl number $Pr_m = \nu/\eta$ must be greater than unity, whereas in the Sun it is significantly less than unity (based on microscopic values

for ν and η). This is a well-known difficulty in dynamo simulations within astrophysical or geophysical contexts (see, e.g., Christensen et al. 1999). However, the diffusivities in our simulations arise from unresolved convective motions, not microscopic processes, and the effective transport properties of such motions are thought to yield Prandtl and magnetic Prandtl numbers of order unity.

3. CONVECTION, ROTATION, AND THE GENERATION OF FIELDS

3.1. Progenitor Nonmagnetic Convection

Figure 1 illustrates the convective structure and differential rotation for the hydrodynamical progenitor case H immediately prior to introducing a seed magnetic field. The radial velocity near the top of the domain is shown using a Mollweide projection, which displays the entire horizontal layer with minimal distortion. The circular arcs ($\pm90°$) encompass a hemisphere, and the rest of the globe is contained in the lunes on either side. The convection patterns are complex, time dependent, and asymmetric owing to the density stratification, consisting of relatively weak, broad upflows with narrow, fast downflows around their periphery. This asymmetry translates into a net downward transport of kinetic energy. The strong correlations between warm upward motions and cool downward motions are essential in transporting heat outward.

There is a clear difference in the size and structure of the convective patterns at low and high latitudes. Near the equator the downflow lanes tend to align with the rotation axis in the north/south direction, whereas at higher latitudes ($\gtrsim25°$) they tend to be more isotropic and of smaller spatial extent. Part of this behavior can be understood by considering the cylinder that is aligned with the rotation axis and tangent to the inner boundary. This tangent cylinder intersects the outer boundary at latitudes of about $42°$. It is well known that in a rotating convective shell the flow dynamics is different inside and outside of the inner tangent cylinder (Busse 1970; Busse & Cuong 1977). The connectivity of the flow, the influence
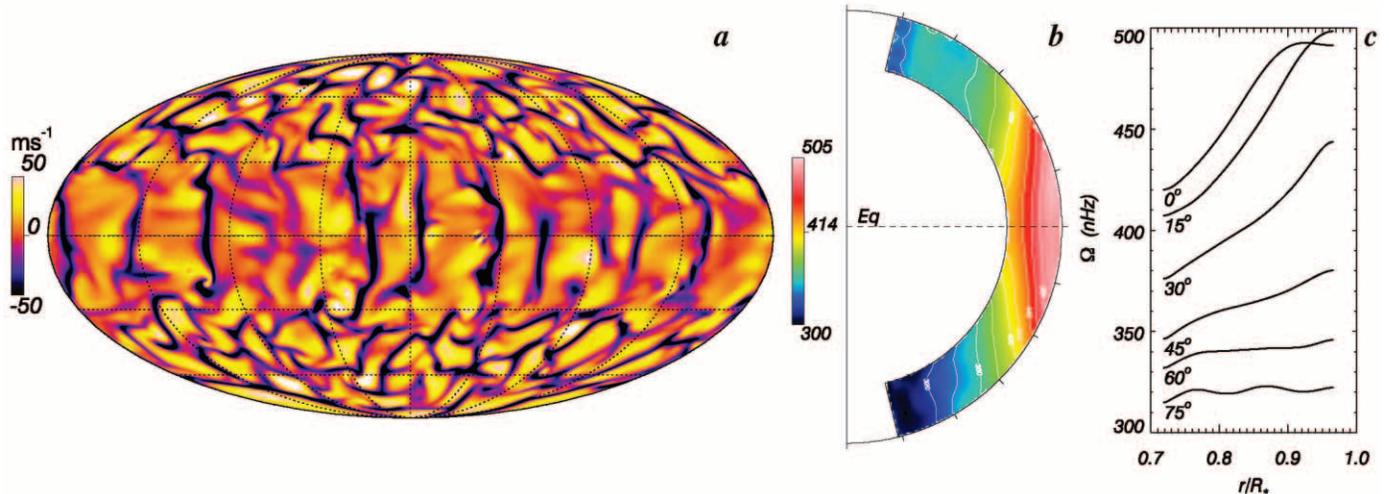
FIG. 1.—(*a*) Radial velocity near the top of the shell for case H shown using a Mollweide projection. Dashed lines indicate the equator, as well as meridians and parallels every 45° and 30°, respectively. Downflows appear dark and upflows bright. (*b*) Angular velocity Ω in case H averaged over longitude and time, with brighter tones indicating more rapid rotation (see color tables). (*c*) Mean angular velocity shown as a function of radius for the indicated latitudes, averaged over both hemispheres.

of Coriolis forces, and the distance to the rotation axis are different in the polar regions relative to the equatorial regions, leading to different convective patterns in mildly turbulent simulations such as case H. At low Reynolds numbers the transition between equatorial modes and polar modes occurs near the tangent cylinder. As the Reynolds number is increased, this transition moves to lower latitudes and becomes less apparent. For example, Brun & Toomre (2002) have demonstrated that increasing the level of turbulence in the simulations makes the convective patterns in the equatorial region more isotropic and extended downflow lanes become difficult to isolate within the convective network.

Vortical plumes are evident at the interstices of the downflow network, representing coherent structures that are surrounded by more chaotic flows. The sense of the vorticity is generally cyclonic: counterclockwise in the northern hemisphere and clockwise in the southern hemisphere. The strongest downflow plumes extend through the entire depth of the domain. They tend to align with the rotation axis and to tilt away from the meridional plane, leading to Reynolds stresses that are crucial ingredients in redistributing the angular momentum within the shell (see § 5; see also Miesch et al. 2000; Brun & Toomre 2002). Downflow lanes and plumes are continually advected, sheared, and distorted by differential rotation and nonlinear interactions with other flow structures.

The differential rotation in case H is shown in Figures 1*b* and 1*c*, expressed in terms of the sidereal angular velocity Ω. The angular velocity of the rotating reference frame is 414 nHz, which corresponds to a rotation period of 28 days. In the contour plot, the polar regions have been omitted owing to the difficulty of forming stable averages there as a result of the small moment arm and small averaging domain.

Case H exhibits a differential rotation profile that is in good agreement with the solar internal rotation profile inferred from helioseismology in the bulk of the convection zone (Thompson et al. 2003). Angular velocity contours at midlatitudes are nearly radial, and the rotation rate decreases monotonically with increasing latitude as in the Sun. The latter property, in particular, represents an important improvement over most previous spherical convection simulations in which the latitudinal angular velocity contrast ΔΩ was confined mainly to

mid- and low latitudes, namely, outside of the inner tangent cylinder. The angular velocity profile in such simulations is generally sensitive to the parameters of the problem, and more solar-like profiles such as case H can be achieved by varying the Reynolds and Prandtl numbers in particular (Elliott et al. 2000; Brun & Toomre 2002). The differential rotation contrast between the equator and latitudes of 60° in case H is 140 nHz (or 34% relative to the frame of reference), somewhat larger than the 92 nHz (or 22%) variation implied by helioseismology. The rotation profile of case H exhibits some asymmetry with respect to the equator, particularly at high latitudes (Fig. 1*b*), although such asymmetries are expected to diminish over a longer temporal average. Since the convection itself is generally asymmetric, it is not surprising that the mean flows driven by the convection are as well.

Mean field models of the solar differential rotation have advocated that a thermal wind balance (involving latitudinal temperature gradients) may be the cause of the noncylindrical angular velocity profile (Kichatinov & Rüdiger 1995; Durney 1999). This may come about if baroclinic convective motions produce latitudinal heat flux, leading to a breakdown of the Taylor-Proudman theorem (Pedlosky 1987). A pole-equator temperature contrast of a few degrees kelvin is compatible with a $\Delta\Omega/\Omega_0$ of ∼30%. Although it is indeed true that case H exhibits latitudinal entropy and temperature gradients, these are not the dominant players in driving the differential rotation throughout the shell. Rather, we find that the Reynolds stresses are the main agents responsible for maintaining the rotation profiles in our simulations (see § 5).

3.2. *Achieving Sustained Dynamo Action*

We now consider the dynamo possibilities that such intricate convective patterns and large differential rotation can lead to. As stated earlier, we have introduced a seed magnetic poloidal field into our hydrodynamical case H for three different values of the magnetic diffusivity *η*, corresponding to cases M1, M2, and M3 (Table 1). Figure 2 shows the magnetic and kinetic energy evolution for these three cases. We note that over more than 4000 days (corresponding to several ohmic decay times; see Table 1) the two least diffusive cases M2 and M3 achieve a sustained magnetic energy (ME), the amplitude of which
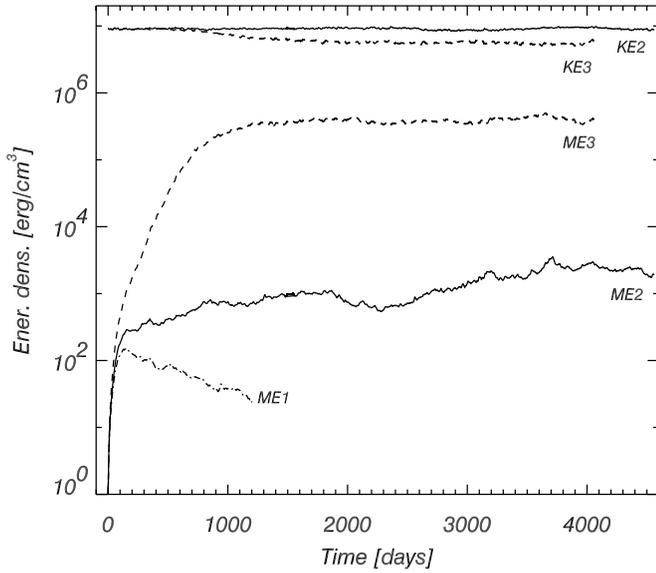
Fig. 2.—Temporal evolution of the volume-integrated kinetic energy density (KE) and magnetic energy density (ME) shown for cases M1 (Re$_m$ = 272), M2 (Re$_m$ = 334), and M3 (Re$_m$ = 486), represented by dot-dashed, solid, and dashed lines, respectively.

depends on η. The initial exponential growth of ME in case M3 lasts for about 600 days, after which the nonlinear feedback of the Lorentz forces on the flow begins to saturate the dynamo. For case M2, which has a slower growth rate, another linear phase seems to last for at least 4000 days, and it is unclear whether it has truly saturated. By contrast, case M1 is clearly decaying, since the rate of generation of magnetic fields in the entire shell volume $[\int_V \boldsymbol{v} \cdot (\boldsymbol{B} \times \boldsymbol{j}) \, dV]$ cannot compensate for the rate of destruction by ohmic diffusion ($\int_V 4\pi\eta/c\boldsymbol{j}^2 \, dV$). Interpolating between cases M1 and M2 to find the zero growth rate yields a critical magnetic diffusivity at midlayer depth $\eta \sim 5.9 \times 10^{11}$ cm s^{-2}. In terms of the magnetic Reynolds number (see Table 1), we find that Re$_m$ must be at least 300 for sustained dynamo action to occur. This value of Re$_m$ is about 25% larger than in the incompressible simulations of Gilman (1983), which consider a simpler configuration.

Upon saturation, the kinetic energy (KE) in model M3 has been reduced by about 40% compared to its initial value, say, KE$_0$, given by case H (see Table 2). This change is mostly due to a reduction of the energy contained in the differential rotation (DRKE), which drops by over 50%. By contrast, the energy contained in the convective motions (CKE) only decreases by about 27%, which implies an increased contribution of the nonaxisymmetric motions to the total kinetic energy balance.

TABLE 2
Representative Velocities, Magnetic Fields, Energies, and Differential Rotation

Parameter	H	M1	M2	M3
Middle of Convective Zone				
$\tilde{v}_r$	61	60	59	58
$\tilde{v}_\theta$	63	62	61	54
$\tilde{v}_\phi$	137	137	136	104
$\tilde{v}'_\phi$	68	68	67	59
$\tilde{v}$	163	162	161	131
$\tilde{v}'$	111	111	109	99
$\tilde{B}_r$	...	21	100	1752
$\tilde{B}_\theta$	...	23	110	1855
$\tilde{B}_\phi$	...	29	144	2277
$\tilde{B}'_\phi$	...	28	141	2239
$\tilde{B}$	...	42	207	3420
$\tilde{B}'$	...	41	205	3386
Volume Average				
KE	9.01×10^6	8.74×10^6	8.96×10^6	5.26×10^6
DRKE/KE (%)	59.3	57.4	57.8	49.5
MCKE/KE (%)	0.3	0.4	0.4	0.5
CKE/KE (%)	40.4	42.2	41.8	50.0
ME	...	$<10^2$	1223	3.47×10^5
ME/KE (%)	...	$<10^{-3}$	0.014	6.6
MTE/ME (%)	...	...	1.4	1.5
MPE/ME (%)	...	...	0.6	0.5
FME/ME (%)	...	...	98	98
$\Delta\Omega/\Omega_0$ (%)	34	34	34	24

Notes.—Listed for each simulation are the rms amplitude of the velocity $\tilde{v}$ and each of its components, $\tilde{v}_r$, $\tilde{v}_\theta$, and $\tilde{v}_\phi$, averaged over time at a layer in the middle of the convection zone. Also listed are the rms amplitudes of the fluctuating total and zonal velocity, $\tilde{v}'$ and $\tilde{v}'_\phi$, obtained after subtracting out the temporal and azimuthal mean. For the magnetic simulations, we include the corresponding rms amplitudes of the magnetic field and its components, $\tilde{B}$, $\tilde{B}_r$, $\tilde{B}_\theta$, $\tilde{B}_\phi$, $\tilde{B}'$, and $\tilde{B}'_\phi$. Velocities are expressed in m s^{-1} and magnetic fields in G. The kinetic energy density KE ($\frac{1}{2}\bar{\rho}v^2$), averaged over volume and time, is also listed along with the relative contributions from nonaxisymmetric convection (CKE), as well as the axisymmetric differential rotation (DRKE) and meridional circulation (MCKE). We also list, where appropriate, the average magnetic energy density ME ($B^2/8\pi$) and the relative contribution from each of its components, including the fluctuating (nonaxisymmetric) field FME and the mean (axisymmetric) toroidal and poloidal fields MTE and MPE. The relative latitudinal contrast of angular velocity $\Delta\Omega/\Omega_0$ between latitudes of $0°$ and $60°$ near the top of the domain is also stated for each case (averaged over both hemispheres).

For case M3, the decrease in KE first becomes apparent after about 600 days of evolution, when the ME reaches roughly 0.5% of KE_0. After 1200 days, the ME reaches a value of about 8% of the KE and retains that level for more than 3 ohmic decay times τ_η. The ME in case M2 is still too small ($\leq 0.1\%$) even after 4000 days for Lorentz forces to have a significant influence on the convective motions, as demonstrated by comparing the kinetic energy evolution in cases M2 and M3.

It is instructive to briefly consider the exchange of energy among different reservoirs in our simulations. We refer to Starr & Gilman (1966) for a more detailed discussion of energy exchange in an MHD system. We first note that both the total kinetic and magnetic energies remain small compared to the total potential, internal, and rotational energies contained in the shell. Further, the magnetic energy must arise from the conversion of kinetic energy, but this does not necessarily lead to a decrease in the total kinetic energy because the motions may draw on other reservoirs. Yet, in all of our magnetic simulations, energy is redistributed such that the sum of the kinetic and magnetic energy is less than the total kinetic energy contained in case H. The net energy deficit can be attributed primarily to the reduction in strength of the differential rotation by Maxwell stresses. This means that in a convection zone the way the energy is redistributed among and within the different reservoirs is modified by the presence of magnetic field, but these modifications remain small in the cases presented here. We refer to Cattaneo et al. (2003) for a detailed study of the influence of an imposed magnetic field on Boussinesq convection.

To further investigate the role played by the different agents in transporting energy, we illustrate in Figure 3 the contribution of various physical processes to the total radial energy flux through the shell, converted to luminosity and normalized to the solar luminosity. The net luminosity, $L(r)$, and its components are defined as

$$F_e + F_k + F_r + F_u + F_v + F_m = \frac{L(r)}{4\pi r^2}, \quad (11)$$

with

$$F_e = \bar{\rho} c_p \overline{v_r T'}, \quad (12)$$

$$F_k = \frac{1}{2}\bar{\rho}\overline{v^2 v_r}, \quad (13)$$

$$F_r = -\kappa_r \bar{\rho} c_p \frac{d\bar{T}}{dr}, \quad (14)$$

$$F_u = -\kappa \bar{\rho} \bar{T} \frac{d\bar{S}}{dr}, \quad (15)$$

$$F_v = -\overline{\boldsymbol{v}\cdot\boldsymbol{\mathcal{D}}}, \quad (16)$$

$$F_m = \frac{c}{4\pi}\overline{E_\theta B_\phi - E_\phi B_\theta}, \quad (17)$$

where $\boldsymbol{E} = 4\pi\eta\boldsymbol{j}c^{-2} - (\boldsymbol{v}\times\boldsymbol{B})c^{-1}$ is the electric current, F_e is the enthalpy flux, F_k is the kinetic energy flux, F_r is the radiative flux, F_u is the unresolved eddy flux, F_v is the viscous flux, and F_m is the Poynting flux. The unresolved eddy flux F_u is the heat flux due to SGS motions, which, in our LES-SGS approach, takes the form of a thermal diffusion operating on the mean entropy gradient. Its main purpose is to transport energy outward through the impenetrable upper boundary where the convective fluxes F_e and F_k vanish and the remaining fluxes are small. It should not be mistaken with F_r, which is the flux due to radiative diffusion and which operates on the mean
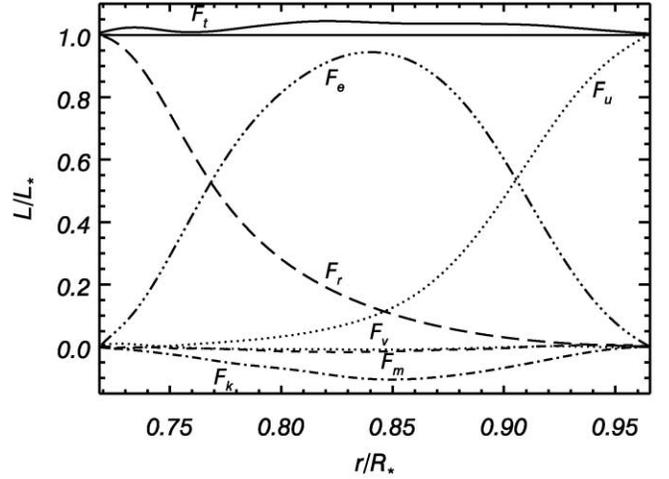
Fig. 3.—Energy flux balance with radius, averaged over horizontal surfaces and in time. The net radial energy flux in case M3 (*solid line*) is expressed as an integrated luminosity through horizontal shells and normalized with respect to the solar luminosity, L_*. In the other curves, this net flux is separated into components as defined in eqs. (11)–(17), including the enthalpy flux F_e, the radiative flux F_r, the unresolved eddy flux F_u, the kinetic energy flux F_k, the Poynting flux F_m, and the viscous flux F_v.

temperature gradient. The radiative diffusivity, κ_r, is derived from a one-dimensional solar structure model (Brun et al. 2002), whereas the eddy diffusivity κ is chosen to model the effects of small-scale motions and to ensure that the flow is well resolved. There is an additional energy flux, F_v, which arises from the SGS eddy viscosity, ν.

If the simulation were in a thermally relaxed state, the total flux through each horizontal surface would be constant and equal to the solar luminosity that is applied at the upper and lower boundaries: $L(r) = L_*$. Figure 3 indicates that the normalized net flux L/L_* (*solid line*) is indeed close to unity, implying that the simulation is close to thermal equilibrium.

The enthalpy flux here carries up to 90% of the solar luminosity in the bulk of the convective zone, and F_r and F_u carry the energy at, respectively, the bottom and top of the domain where F_e vanishes. The remaining fluxes F_k, F_v, and F_m are relatively small and negative in most of the domain. The downward direction of the kinetic energy flux is due to the asymmetry between the fast downflow lanes and the slower broad upflows. This downward flux carries about 10% of the solar luminosity and possesses a bigger amplitude than either F_v or F_m. The low amplitude of F_v confirms that in our simulations inertia dominates over viscous effects, i.e., the Reynolds number in all cases is much greater than unity. Similarly, the low amplitude of the Poynting flux confirms that magnetic processes in case M3 do play a role in the overall energy transport but not to the point of significantly modifying the flux balance established in the nonmagnetic progenitor case H. The volume-integrated ME is about 10% of KE; it would likely require a much higher level of magnetism in order for the Poynting flux to have a substantial influence on the net energy transport.

The Poynting flux F_m is also influenced by our choice of magnetic boundary conditions. In all the magnetic cases presented here we match the computed field to an internal and external potential field at every time step. This leads to a nonzero electromagnetic flux through the boundaries. We have investigated the impact of such magnetic energy "leakage" on the dynamo action by computing one case in which the magnetic field was required to be purely radial at the boundaries, yielding
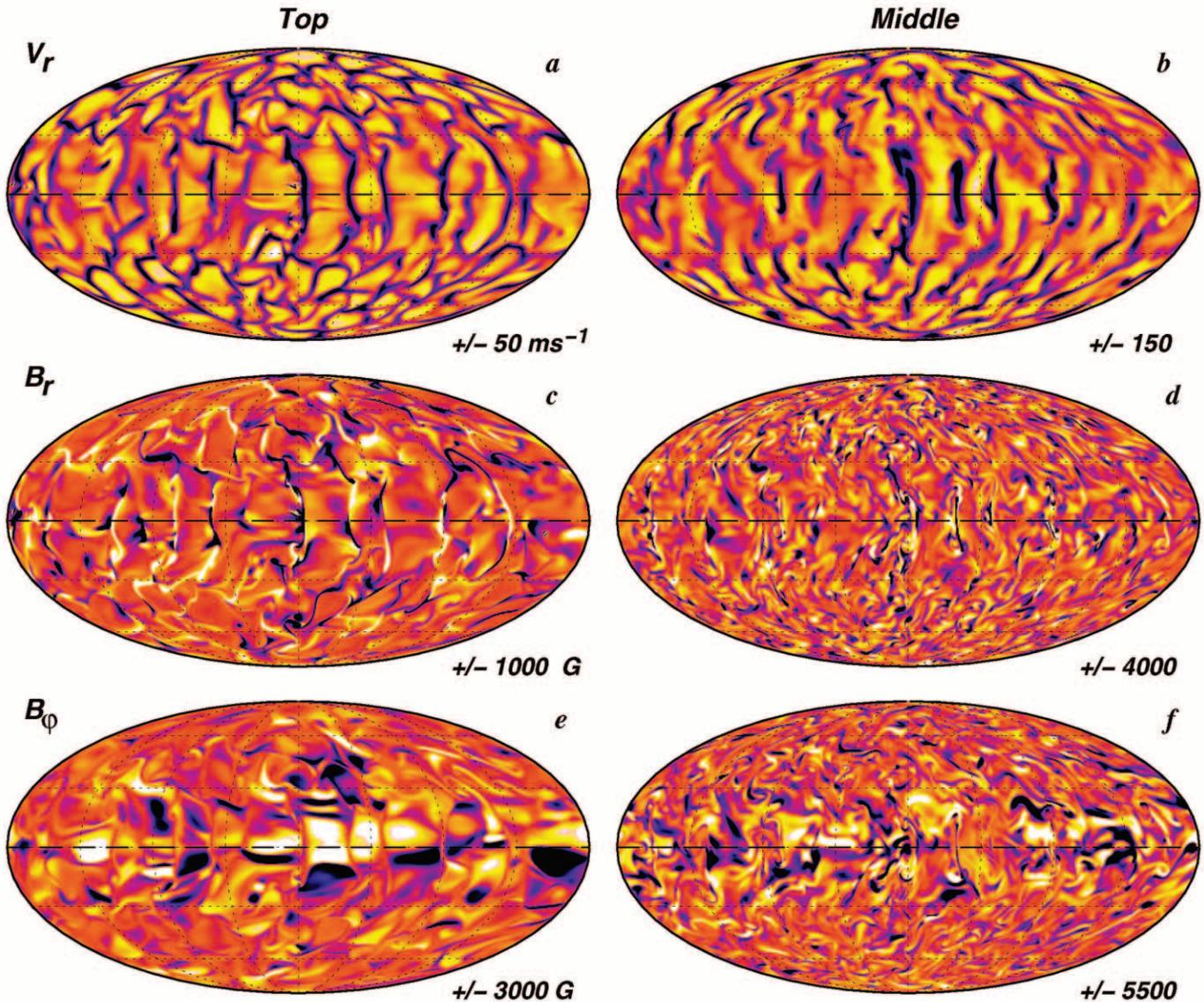
FIG. 4.—Global views at one instant in time of the radial velocity component (*top panels*) and the radial and longitudinal magnetic field components (*middle and bottom panels*) in case M3 near the top (*left panels*) and middle (*right panels*) of the computational domain. Dark tones in turn represent downflow, inward, and westward fields, with the ranges for each color table indicated. The color table is as in Fig. 1.

no net Poynting flux through the shell ($F_m = 0$ at the top and bottom boundaries). The effect of closed as opposed to open boundary conditions seems to be that in the former the magnetic energy amplification is more efficient, with potentially a lower dynamo threshold. But since in the solar case such magnetic energy "leakage" exists both at the bottom via, for example, turbulent pumping (Tobias et al. 2001) and at the photosphere via, for example, magnetic eruptions, we consider that our choice of boundary conditions is reasonable for the solar dynamo problem. We further believe that open magnetic boundary conditions play a central role in regulating the magnetic dynamo action in the convection zone, by providing an outlet for the magnetic energy and also most likely for the magnetic helicity.

4. CONVECTIVE AND MAGNETIC STRUCTURES

4.1. *Flow Patterns and Their Evolution*

The structure of the convection in simulation M3 is illustrated in Figure 4. The convective patterns are qualitatively

similar to the hydrodynamic case H, which can be seen by comparing the radial velocity field in the top left panel of Figure 4 to that shown in Figure 1. Cases M1 and M2 also exhibit similar patterns because the magnetic fields in these simulations never grow strong enough to exert a substantial influence on the global flow structure. However, Lorentz forces in localized regions of case M3 do have a noticeable dynamical effect, particularly with regard to the evolution of strong downflow lanes where magnetic tension forces can inhibit vorticity generation.

The horizontal structure of the radial and longitudinal magnetic field is also shown in Figure 4. Many of the main features are qualitatively similar to simulations of turbulent, compressible magnetoconvection in Cartesian geometries (Cattaneo 1999; Stein & Nordlund 2000; Tobias et al. 2001). The magnetic field generally has a finer and more intricate structure than the velocity field because of the smaller diffusion ($\mathrm{Pr}_m = \nu/\eta = 4$ in this simulation) and also the nature of the advection terms in the induction equation, which are similar in
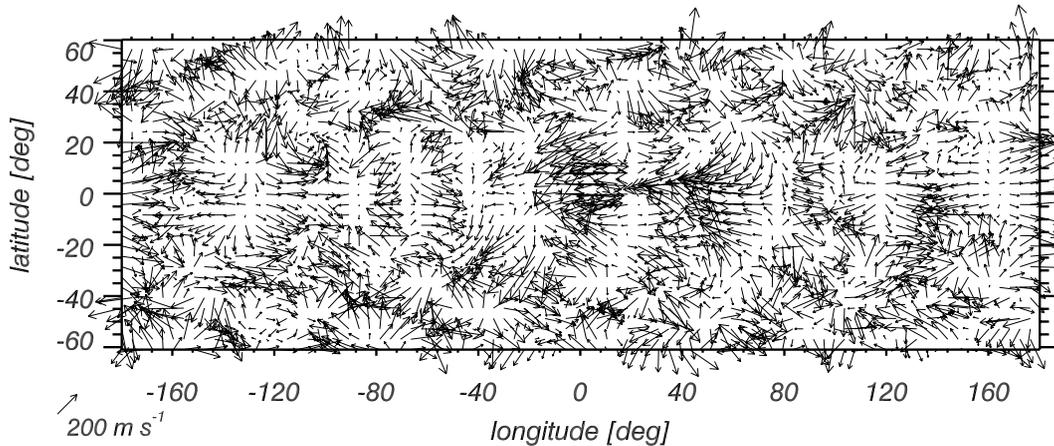
form to those in the vorticity equation (e.g., Biskamp 1993). Near the top of the shell, the radial magnetic field B_r is mainly concentrated in the downflow lanes, where both polarities coexist in close proximity. By contrast, the toroidal field B_ϕ near the surface appears more distributed and more patchy, characterized by relatively broad regions of uniform polarity, particularly near the equator. The magnetic field topology generally does not exhibit any clear symmetries about the equator, although some of the B_ϕ patches at low latitudes do have an antisymmetric counterpart.

In the middle of the shell the magnetic fluctuations appear of smaller scale and more distributed, but they are still very intermittent. Strong vertical fields of mixed polarity still correlate well with downflow lanes and plumes. The longitudinal field is more filamentary and is organized in longitudinally elongated structures, having been stretched by the gradients in angular velocity (see also § 4.2).

Throughout the shell, the magnetic field patterns evolve rapidly, as fields are continuously transported, distorted, and amplified by convective motions. Of particular importance near the top of the shell are the horizontal flows, shown in Figure 5 for case M3. Regions of convergence and divergence are apparent, as are swirling vortices, which occur most frequently at mid- and high latitudes and generally have a cyclonic sense (counterclockwise in the northern hemisphere and clockwise in the southern). Such flows stretch the horizontal field and sweep the vertical field into vortical downflow lanes where it is twisted, thus generating magnetic helicity. Horizontally converging flows also squeeze together fields of mixed polarity, driving magnetic reconnection.

The convective patterns visible in the vertical velocity field of Figure 4 are also evident in the horizontal velocity patterns of Figure 5, particularly the dichotomy between low latitudes, which are dominated by extended downflow lanes oriented north-south (visible here as lines of horizontal convergence), and higher latitudes, which possess a smaller scale, more isotropic downflow network. If they exist in the Sun, such large-scale convective patterns may ultimately be detectable in similar horizontal flow maps inferred from local-domain helioseismic analyses using time-distance and ring-diagram procedures (e.g., Haber et al. 2002; Hindman et al. 2004). However, currently such helioseismic flow maps are limited to the upper few percent of the solar envelope, monitoring SSW

(Toomre 2002). This lies outside the computational domain considered here.

The dynamical richness and rapid time evolution of the flow and magnetic field patterns are highlighted in Figure 6. The radial magnetic field, the radial velocity field, and the horizontal flow all exhibit an intricate structure that evolves substantially on timescales of weeks and even days. Low-latitude features tend to drift eastward relative to higher latitude features as a result of advection by the differential rotation and also inherent pattern propagation relative to the local rotation rate. At the tracking rate used in Figure 6, this leads generally to a rightward movement of patterns near the equator and a leftward movement of patterns near the southern edge of the region shown (latitude −60°). In between, particularly at a latitude of about −25°, the distinctive patterns at low and high latitudes meet, giving rise to a particularly complex dynamical evolution. The north-south aligned downflow lanes at low latitudes temporarily link to the high-latitude network as they drift by, and features caught in this interaction region are rapidly sheared and distorted, forming filaments and vortices that then mix and merge with other structures.

Figure 6 highlights the evolution of several features in particular, indicated by letters. The first of these, A, is a multipolar region that appears to represent several flux tubes passing through the horizontal plane being visualized. After they form, these localized features are rapidly sheared by convective motions, distorting and separating into flux sheets that then merge with other features and lose their identity over the course of about 2 weeks. Feature B begins as a flux sheet confined to a north-south oriented downflow lane where the polarity of the field is radially inward. By the second frame, flux of the opposite polarity (radially outward; indicated by white) is advected into the downflow lane where it is then wrapped up by the cyclonic vorticity and rapidly dissipated as it reconnects with the existing field. Similar dynamics are also occurring in feature C, which illustrates the merging of two flux sheets of opposite polarity in a downflow lane (particularly evident in the rightmost frame). The lower portion of the outward-polarity sheet (*white*) extends into the interface region at latitude −25°, where extended low-latitude downflow lanes merge with the high-latitude network. The intense vorticity and shear in this region twist and stretch the field, dramatically changing its appearance on a timescale of several days.
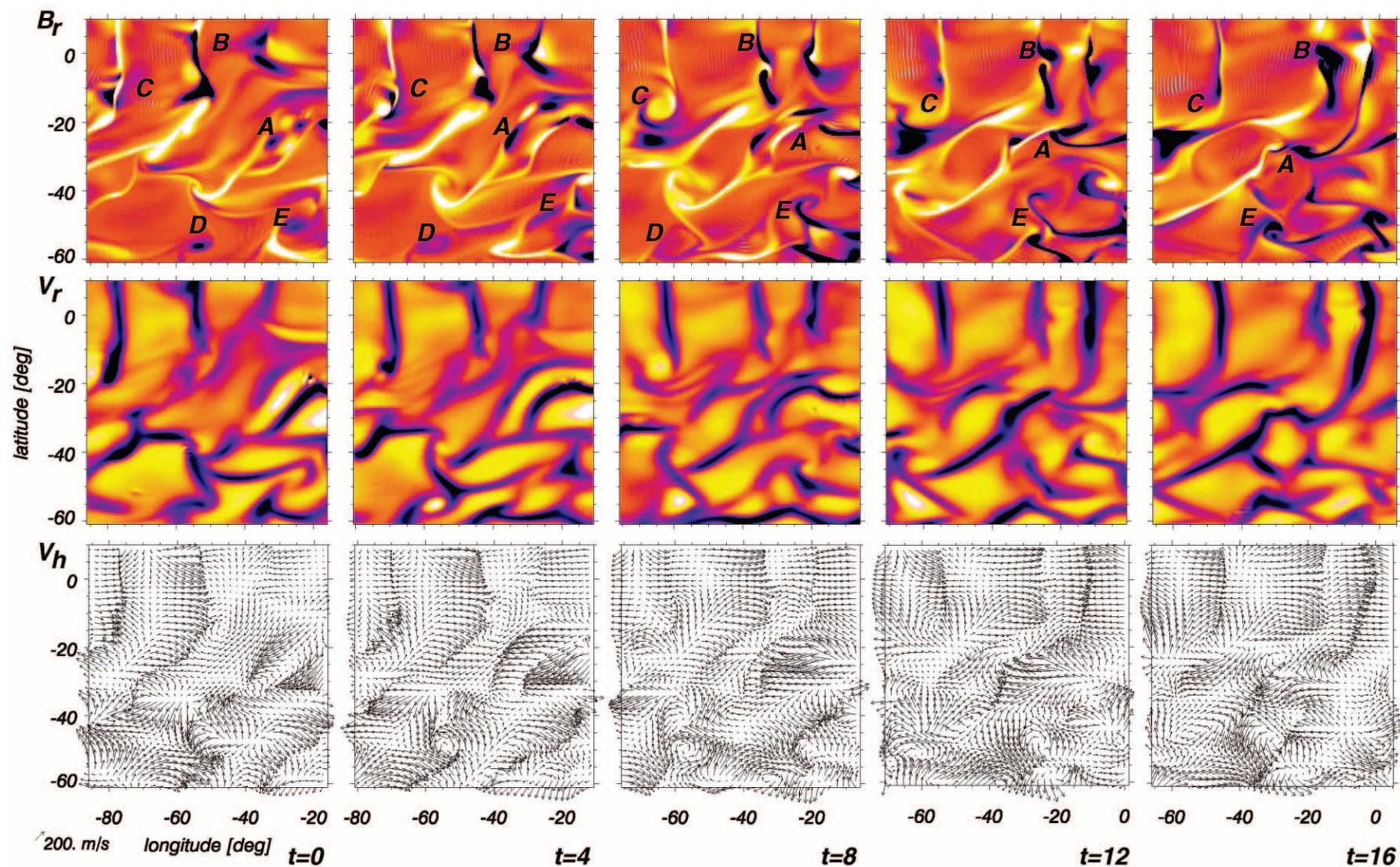
FIG. 6.—Radial magnetic field (B_r; *top panels*), radial velocity (v_r; *middle panels*), and horizontal flow vectors (v_h; *bottom panels*) shown for a selected horizontal domain near the top of the shell in case M3. A sequence of five snapshots is shown, each separated by an interval of 4 days, with time increasing from left to right. This region spans 70° in both latitude and longitude; the longitude range shifts eastward by 5° with each successive snapshot in order to track some of the flow features. Particular features are indicated with labels. The horizontal level and the time of the first snapshot correspond to the global views shown in the left panels of Fig. 4 and in Fig. 5. The color table is the same as in Fig. 1.
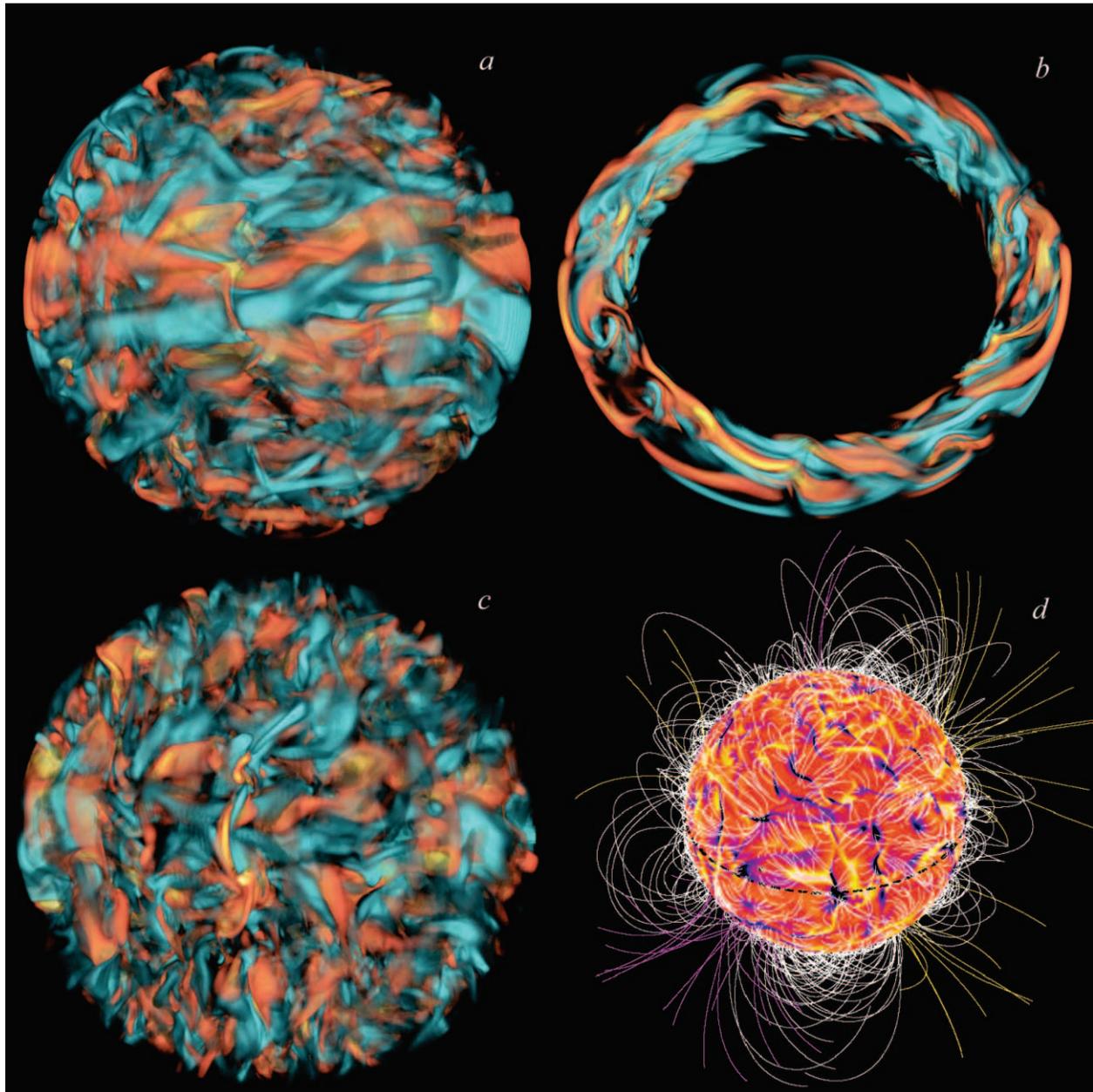
FIG. 7.—(*a*, *c*) Volume renderings of the toroidal (B_ϕ) and radial (B_r) magnetic fields in case M3 at one instant in time (the same as in Fig. 4). Red tones indicate outward and eastward (prograde) fields, and blue tones denote inward and westward (retrograde) fields. (*b*) Selected subvolume of B_ϕ including the full span of longitude and radius but only a narrow band in latitude centered around the equator. The equatorial plane is tilted nearly perpendicular to the viewing in order to highlight the radial and longitudinal structure. Typical field strengths are about 1000 G for B_r and 3000 G for B_ϕ. (*d*) Potential field extrapolation of the radial magnetic field at the top of the computational domain. The radial field at the surface is shown in an orthographic projection, and the visualization traces individual field lines indicated in white if they form closed loops and in yellow or magenta if they represent an open field of positive (outward) or negative (inward) polarity, respectively.

The most intense downflow plumes often possess enough vorticity to evacuate the core of the plume owing to centrifugal forces, and buoyancy forces acting on the resulting decrease in density lead to a flow reversal, creating a new upflow region that then diverges horizontally as a result of the density stratification (Brandenburg et al. 1996; Brummell et al. 1998; Miesch et al. 2000). Such dynamics is occurring in feature D of Figure 6, now in the presence of a magnetic field. By the second frame, a new upflow is created in this manner (*middle panels*) that rapidly expands horizontally and interacts with the surrounding flow. There is a vertical flux tube present in the original downflow, but it is rapidly dispersed as the flow reverses, losing all coherence by the fourth frame. Feature E is another example of how the field can be wrapped up by the vorticity in downflow lanes, particularly at mid- and high latitudes where the rotation vector has a large vertical component.

4.2. *Morphology of Magnetic Fields*

Horizontal cross sections as in Figures 4–6 are informative, but they provide limited insight into the three-dimensional structure of the flow and of the magnetic field in particular. Further insight requires volume visualizations as shown in Figure 7.

The toroidal and radial magnetic fields in Figures 7*a* and 7*c* have a very different appearance, consistent with the contrast noted previously in Figure 4. Whereas B_r is concentrated into

vertically oriented sheets and filaments, B_ϕ is organized into relatively broad ribbons and tubes that extend mainly in longitude. Figure 7b further demonstrates the ribbon-like topology of the toroidal field, showing in particular that the low-latitude horizontal patches near the surface have a relatively small vertical extent, although some meander in radius. Substantial magnetic helicity is present throughout, involving complex winding of the toroidal field structures along their length. Some features resemble magnetic flux tubes, but they generally do not remain coherent long enough for magnetic buoyancy forces to induce them to rise.

Whereas some toroidal field structures maintain coherence over global scales, the radial field is generally dominated by smaller scale fluctuations. In particular, radial field structures near the top of the domain rarely penetrate deep into the convection zone, although individual field lines maintain some connectivity throughout the shell. This connectivity also extends outside of the computational domain because of the boundary conditions that match the interior field to an external potential field. The structure of this potential field above the outer surface is illustrated in Figure 7d. The extrapolation shown in the figure treats the radial field near the top of the domain as a source surface and requires that the field be radial at $2.5R_*$, although field lines are only shown out to a radius of $1.5R_*$.

As in the Sun, the surface magnetic field is complex, featuring bipolar regions, nested loops, and an intricate web of connectivity between both local and widely separated regions on the surface. Although some large loops span both hemispheres, dipolar or quadrupolar components are not evident and open field is not confined to or even preferred in the polar regions. Axisymmetric field components are indeed present (see § 6), but the field morphology near the surface and throughout the shell is dominated by smaller scale turbulent structures.

The magnetic energy in the potential field extrapolation decreases rapidly with increasing radius, as spherical harmonic components decay in proportion to $r^{-(l+1)}$. A less dramatic outward gradient of magnetic energy also occurs within the computational domain as demonstrated in Figure 8. Here we display the radial profile of the total magnetic energy density integrated over the horizontal dimensions after having broken it down into mean (axisymmetric) and fluctuating (nonaxisymmetric) poloidal and toroidal components in the following manner:

$$\text{MTE} = \frac{1}{8\pi}\langle B_\phi\rangle^2, \tag{18}$$

$$\text{MPE} = \frac{1}{8\pi}\left(\langle B_r\rangle^2 + \langle B_\theta\rangle^2\right), \tag{19}$$

$$\text{FTE} = \frac{1}{8\pi}\left[\left(B_\phi - \langle B_\phi\rangle\right)^2\right], \tag{20}$$

$$\text{FPE} = \frac{1}{8\pi}\left[(B_r - \langle B_r\rangle)^2 + (B_\theta - \langle B_\theta\rangle)^2\right], \tag{21}$$

$$\text{FME} = \frac{1}{8\pi}\left[(B_r - \langle B_r\rangle)^2 + (B_\theta - \langle B_\theta\rangle)^2 + \left(B_\phi - \langle B_\phi\rangle\right)^2\right], \tag{22}$$

where the angle brackets denote a longitudinal average.

The magnetic energy generally peaks toward the bottom of the shell for both the mean and fluctuating field components. This is due in part to the spherical divergence and the density stratification. Downward pumping of magnetic fields by con-
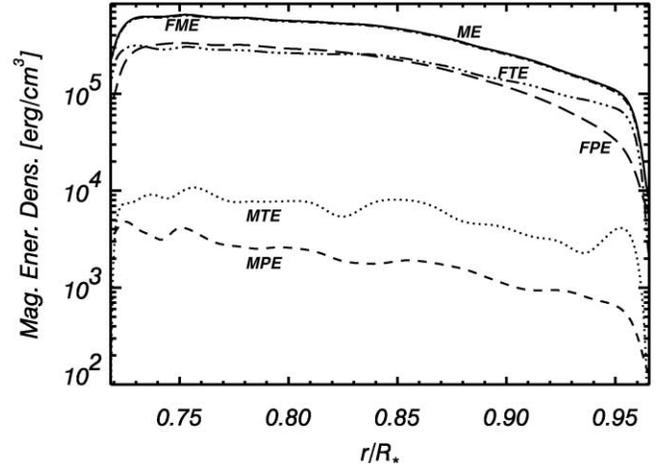
Fig. 8.—Radial profiles of the magnetic energy in case M3. Shown are integrals over horizontal surfaces and averages in time of the total magnetic energy (ME), the energy in the mean (axisymmetric) toroidal field (MTE) and the mean poloidal field (MPE), and the energy in the fluctuating (nonaxisymmetric) fields, including the toroidal component (FTE), the poloidal component (FPE), and their sum (FME).

vective motions also plays a role, but the pumping is not as effective as in penetrative convection simulations where the underlying stable region provides a reservoir where the field can be accumulated and stored (see Tobias et al. 2001).

Figure 8 also shows that the magnetic energy contained in the mean field components is more than an order of magnitude smaller than that contained in the nonaxisymmetric fluctuations. Most of the mean field energy is in the toroidal field, which exceeds the energy in the poloidal field by about a factor of 3 owing to the stretching and amplification of toroidal field by differential rotation (the ω-effect). This ratio is smaller than in the Sun, where the mean toroidal field is estimated to be about 2 orders of magnitude more energetic than the mean poloidal field. This discrepancy can again be attributed to the absence of an overshoot region and a tachocline, where the toroidal field can be stored for extended periods while it is amplified by relatively large angular velocity gradients (see § 6). For the nonaxisymmetric fluctuations, the magnetic energy is approximately equally distributed among the toroidal and poloidal fields, indicating that the turbulent convection can efficiently generate both components in roughly equal measure, implying that the ω-effect plays a lesser role.

5. DIFFERENTIAL ROTATION AND MERIDIONAL CIRCULATION

Surface measurements and helioseismic inferences of large-scale, axisymmetric, time-averaged flows in the Sun currently provide the most important observational constraints on global-scale models of solar convection. The structure, evolution, and maintenance of mean flows (averaged over longitude and time) have therefore been a primary focus of previous global convection simulations (Glatzmaier 1987; Miesch et al. 2000; Elliott et al. 2000; Brun & Toomre 2002). Of particular importance is the mean longitudinal flow, i.e., the differential rotation, which is now reasonably well established from helioseismic inversions, although investigations continue to scrutinize its detailed spatial structure and temporal evolution (Thompson et al. 2003). The mean circulation in the meridional plane has only been probed reliably in the surface layers of the Sun through Doppler measurements (Hathaway et al. 1996) and
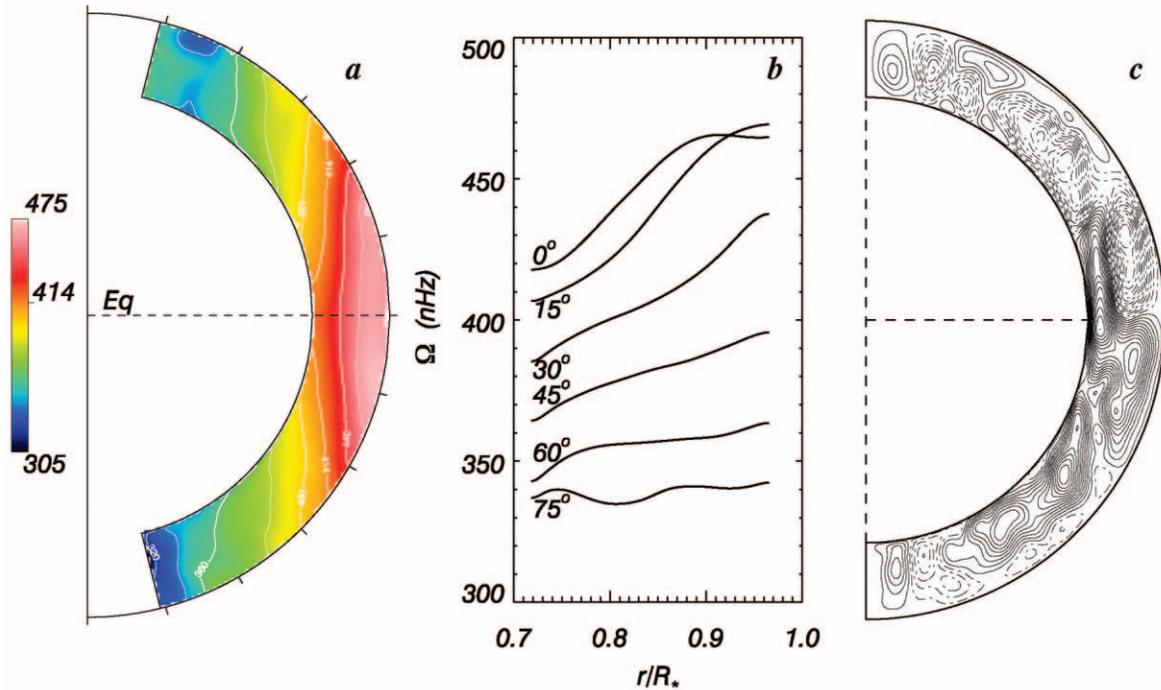
Fig. 9.—(*a*, *b*) Angular velocity profile in case M3 averaged over longitude and time (spanning an interval of 150 days late in the simulation). White/red and blue/green tones in (*a*) denote faster and slower rotation, respectively. Radial profiles are plotted in (*b*) for selected latitudes. (*c*) Meridional circulation in case M3 averaged over longitude and time, represented as streamlines of the mass flux. Solid contours denote clockwise circulation and dashed contours counterclockwise circulation.

local-area helioseismology (e.g., Haber et al. 2002). Here we discuss the mean flows achieved in our simulations and compare them with solar observations and previous numerical models.

5.1. *Attributes of Mean Flows*

With fairly strong magnetic fields sustained within the bulk of the convection zone in case M3, it is to be expected that the differential rotation Ω will respond to the feedback from the Lorentz forces. Figure 9*a* shows the time-averaged angular velocity achieved in case M3, which exhibits a prograde equatorial rotation with a monotonic decrease in angular velocity toward higher latitudes as in the Sun. The main effect of the Lorentz forces is to extract energy from the differential rotation. The kinetic energy contained in the differential rotation drops by a factor of 2 after the addition of magnetic fields, and this decrease accounts for over 70% of the total kinetic energy difference (see § 3.2). This is reflected by a 30% decrease in the angular velocity contrast $\Delta\Omega$ between the equator and latitudes of 60°, going from 140 nHz (or 34% compared to the reference frame Ω_0) in the hydrodynamic case H to 100 nHz (or 24%) in case M3. This value is close to the contrast of 22% inferred from helioseismic inversion of the solar profile (Thompson et al. 2003). Thus, the convection is still able to maintain an almost solar-like angular velocity contrast despite the inhibiting influence of Lorentz forces.

Eddy et al. (1976) have deduced from a careful study of solar activity records during the Maunder minima that the Sun was rotating about 3%–4% faster in the equatorial region during that period than it does at present and that the angular velocity contrast between the equator and latitudes of 20° may have been as much as a factor of 3 larger. The somewhat faster rotation rate and larger $\Delta\Omega$ in case H (and M2) relative to case M3 further suggest that a reduced level of the Sun's magnetism may lead to greater differential rotation (Brun 2004).

In Figure 9*c* we display the meridional circulation realized in case M3. This meridional circulation is maintained by buoyancy forces, Reynolds stresses, pressure gradients, Maxwell stresses, and Coriolis forces acting on the differential rotation. Since these relatively large forces nearly cancel one another, the circulation can be thought of as a small departure from (magneto)geostrophic balance, and the presence of a magnetic field can clearly influence its subtle maintenance. In case M3, the meridional circulation exhibits a multicell structure in both latitude and radius and possesses some asymmetry with respect to the equator. In particular, two vertical cells are present at low latitudes in the northern hemisphere, whereas only one is present in the southern hemisphere. Since the convection possesses some asymmetry (cf. Fig. 4), it is not surprising that the meridional circulation does the same.

Given the competing processes for its origin, this weak flow is not straightforward to predict. Typical amplitudes for the velocity are of order 25 m s^{-1}, comparable to local helioseismic deductions (Haber et al. 2002). The flow near the outer boundary is directed poleward at low latitudes, with return flow deeper down. The temporal fluctuations in the meridional circulation are large and thus stable time averages are only attained by frequent sampling over many rotation periods. The kinetic energy contained in the meridional circulation (MCKE) is about 2 orders of magnitude smaller than that contained in the differential rotation and convective motions and is more than an order of magnitude less than the total magnetic energy (ME; see Table 2). As a result, small fluctuations in the convective motions, differential rotation, and Lorentz forces can lead to major variations in the circulation. Some of the helioseismic inferences suggest the presence of single-cell circulations, which are at odds with our multicell patterns. However, these inferences vary from year to year and there is recent evidence that multicell structure and equatorial asymmetries are

developing in the meridional circulation patterns just below the photosphere as the current solar cycle advances (Haber et al. 2002).

5.2. *Redistribution of Angular Momentum*

We can better understand how the differential rotation profile in case M3 is achieved by identifying the main physical processes responsible for redistributing angular momentum within our rotating convective shells. Our choice of stress-free and potential-field boundary conditions at the top and bottom of the computational domain has the advantage that no net external torque is applied, and thus angular momentum is conserved. We may assess the transport of angular momentum within these systems by considering the mean radial ($\mathcal{F}_r$) and latitudinal ($\mathcal{F}_\theta$) angular momentum fluxes, extending the procedure used in Brun & Toomre (2002) to the magnetic context (see also Elliott et al. 2000). Let us consider the ϕ-component of the momentum equation expressed in conservative form and averaged in time and longitude (denoted by hat):

$$\frac{1}{r^2}\frac{\partial(r^2\mathcal{F}_r)}{\partial r} + \frac{1}{r\sin\theta}\frac{\partial(\sin\theta\mathcal{F}_\theta)}{\partial\theta} = 0, \tag{23}$$

involving the mean radial angular momentum flux

$$\mathcal{F}_r = \bar{\rho} r\sin\theta\left[-\nu r\frac{\partial}{\partial r}\left(\frac{\hat{v}_\phi}{r}\right) + \widehat{v_r'v_\phi'} + \hat{v}_r\left(\hat{v}_\phi + \Omega r\sin\theta\right)\right.$$
$$\left.-\frac{1}{4\pi\bar{\rho}}\widehat{B_r'B_\phi'} - \frac{1}{4\pi\bar{\rho}}\hat{B}_r\hat{B}_\phi\right] \tag{24}$$

and the mean latitudinal angular momentum flux

$$\mathcal{F}_\theta = \bar{\rho} r\sin\theta\left[-\nu\frac{\sin\theta}{r}\frac{\partial}{\partial\theta}\left(\frac{\hat{v}_\phi}{\sin\theta}\right) + \widehat{v_\theta'v_\phi'} + \hat{v}_\theta\left(\hat{v}_\phi + \Omega r\sin\theta\right)\right.$$
$$\left.-\frac{1}{4\pi\bar{\rho}}\widehat{B_\theta'B_\phi'} - \frac{1}{4\pi\bar{\rho}}\hat{B}_\theta\hat{B}_\phi\right]. \tag{25}$$

In the above expressions for both fluxes, the terms on the right-hand side denote contributions, respectively, from viscous diffusion (which we denote as $\mathcal{F}_r^{\mathrm{VD}}$ and $\mathcal{F}_\theta^{\mathrm{VD}}$), Reynolds stresses ($\mathcal{F}_r^{\mathrm{RS}}$ and $\mathcal{F}_\theta^{\mathrm{RS}}$), meridional circulation ($\mathcal{F}_r^{\mathrm{MC}}$ and $\mathcal{F}_\theta^{\mathrm{MC}}$), Maxwell stresses ($\mathcal{F}_r^{\mathrm{MS}}$ and $\mathcal{F}_\theta^{\mathrm{MS}}$), and large-scale magnetic torques ($\mathcal{F}_r^{\mathrm{MT}}$ and $\mathcal{F}_\theta^{\mathrm{MT}}$). The Reynolds stresses are associated with correlations of the fluctuating velocity components that arise from organized tilts within the convective structures, especially in the downflow plumes (e.g., Brummell et al. 1998; Miesch et al. 2000). In the same spirit the Maxwell stresses are associated with correlations of the fluctuating magnetic field components that arise from tilt and twist within the magnetic structures.

In Figure 10 we show the components of $\mathcal{F}_r$ and $\mathcal{F}_\theta$ for case M3, having integrated over colatitude and radius as follows:

$$I_r(r) = \int_0^\pi \mathcal{F}_r(r,\ \theta)r^2\sin\theta\,d\theta,$$
$$I_\theta(\theta) = \int_{r_{bot}}^{r_{top}} \mathcal{F}_\theta(r,\ \theta)r\sin\theta\,dr. \tag{26}$$

Thus, I_r represents the net angular momentum flux through horizontal shells at different radii and I_θ represents the net flux through cones at different latitudes. We then identify in turn the contributions from viscous diffusion (VD), Reynolds stresses (RS), meridional circulation (MC), Maxwell stresses (MS), and large-scale magnetic torques (MT). This representation is helpful in assessing the sense and amplitude of angular momentum transport within the convective shells by each component of $\mathcal{F}_r$ and $\mathcal{F}_\theta$.

Turning first to Figure 10a, we see that the radial differential rotation is being maintained by Reynolds stresses and meridional circulation, I_r^{RS} and I_r^{MC}, which both transport angular momentum radially outward. This outward transport is opposed by the viscous flux I_r^{VD}, which is radially inward as implied by the positive radial angular velocity gradient seen in Figure 9b. The Maxwell stresses I_r^{MS} also act to oppose the generation of differential rotation by the convection, possessing the same sign and amplitude as the viscous torque. The large-scale magnetic torques are very small but negative as well, helping to decelerate the surface and speed up the bottom of the shell. The net radial flux I_r, represented by the solid line, is nearly zero, indicating that the flow has achieved an approximate statistical equilibrium and that our sampling in time captures this equilibrated state reasonably well, despite the large temporal variations typically present in our simulations.

The latitudinal angular momentum flux I_θ exhibits a more complicated interplay among its various components than I_r, as demonstrated in Figure 10b. Here the angular momentum transport is dominated by Reynolds stresses I_θ^{RS} that are consistently directed toward the equator (i.e., negative in the southern hemisphere and positive in the northern hemisphere). This feature implies that the equatorial acceleration observed in our simulations is mainly due to the transport of angular momentum by the Reynolds stresses. Further, unlike the radial angular momentum balance, we see that the transport by meridional circulation I_θ^{MC} is opposite to F_θ^{RS}, with the meridional circulation seeking to slow down the equator and speed up the poles. The viscous torque I_θ^{VD} is in the same direction but is a factor of 4 smaller in amplitude. These results are identical to that deduced from case H (much as in Brun & Toomre 2002). The main difference in case M3 comes from the Maxwell stress component I_θ^{MS}, which opposes the Reynolds stresses as in the radial angular momentum balance. The large-scale magnetic torque I_θ^{MT} is again found to be negligible. The total flux I_θ vacillates around zero, indicating no net latitudinal angular momentum transport and an acceptable equilibrated solution.

The reduction in the latitudinal contrast of Ω between cases H and M3 can be partially attributed to a global decrease in the kinetic energy of the convection (see Table 2). The rms Reynolds number of case M3 is about 12% less than in case H, reflecting the stabilizing influence of magnetic fields. However, the convection kinetic energy is only reduced by about 27%, whereas the differential rotation kinetic energy is reduced by over 50%. Figure 10 indicates that this large decrease in DRKE is due to the poleward transport of angular momentum by Maxwell stresses. In case M3 the Reynolds stresses must balance the angular momentum transport by the meridional circulation, the viscous diffusion, and the Maxwell stresses, which leads to a less efficient acceleration of the equatorial regions. Since the magnetic energy is only about 7% of the kinetic energy in case M3 (see Table 2), the Maxwell stresses are not the main players in redistributing the angular momentum, but they do contribute more than the viscous torque I_θ^{VD} in the latitudinal balance. If the magnetic energy were to exceed about 20% of the total kinetic energy, Maxwell stresses and
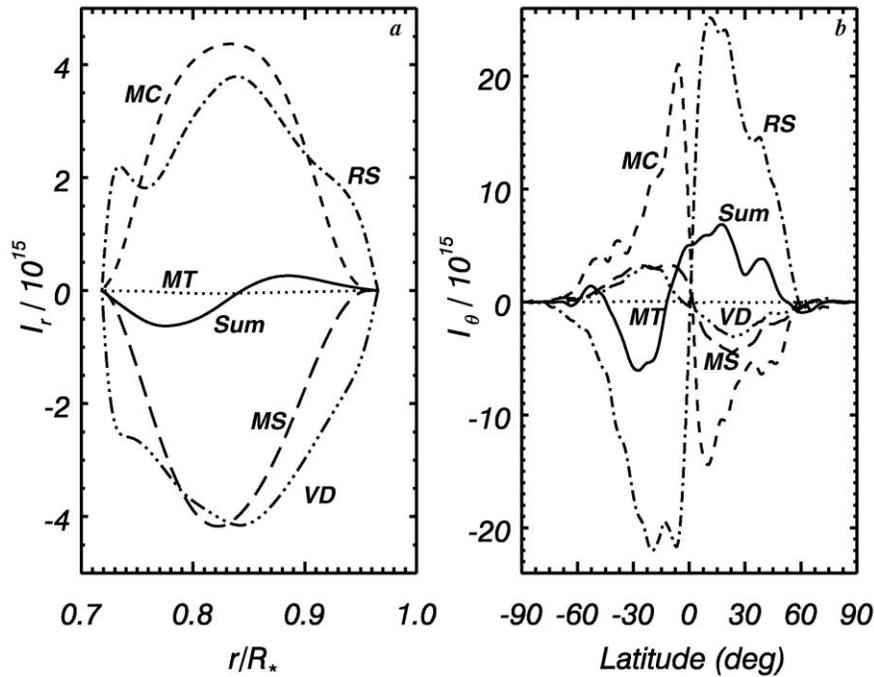
FIG. 10.—Temporal average of (a) the integrated vertical angular momentum flux I_r and (b) the integrated latitudinal angular momentum flux I_θ for case M3. The fluxes have been decomposed into their viscous diffusion (labeled VD), Reynolds stress (RS), meridional circulation (MC), Maxwell stress (MS), and large-scale magnetic torque (MT) components. The solid lines represent the sum of these components and serve to indicate the quality of stationarity achieved. Positive values represent a radial flux that is directed outward and a latitudinal flux directed from north to south. The interval chosen for the time averages spans 150 days late in the simulation (as in Fig. 9). The radial integrated flux I_r has been normalized by r_{top}^2.

magnetic torques may become strong enough to suppress the differential rotation almost entirely (Gilman 1983; Brun 2004). The Sun may have ways of avoiding this by expelling some of its magnetic flux.

We emphasize that the suppression of vertical and latitudinal differential rotation by Lorentz forces in our simulations is dominated by the fluctuating magnetic field components I^{MS}, not the mean field components I^{MT}. Magnetic tension forces associated with the mean poloidal field do tend to inhibit rotational shear as in axisymmetric models (MacGregor & Charbonneau 1999), but this intuitive "rubber band" effect is far less efficient than the more subtle Maxwell stresses induced by correlations among the turbulent magnetic field components.

Brun & Toomre (2002) have found that as the level of turbulence is increased, I^{VD} reduces in amplitude and the transport of angular momentum by the Reynolds stresses I^{RS} and by the meridional circulation I^{MC} changes accordingly to maintain equilibrium. Here the presence of a fourth agent, namely, the Maxwell stresses, can modify this force balance and thus alter the equilibrium rotation profile.

An important feature of the rotation profile in case H and also in case AB of Brun & Toomre (2002) is a monotonic decrease in angular velocity with increasing latitude that persists all the way to the polar regions. This relatively slow polar rotation is supported by helioseismic inversions but is generally difficult to achieve in numerical simulations of convection because regions close to the rotation axis undergo a prograde acceleration if fluid parcels tend to conserve their angular momentum. Thus, it is promising to see that case M3 has retained relatively slow rotation at high latitudes even in the presence of magnetic fields.

Figure 10b indicates that the prograde equatorial rotation seen in case M3 is due to equatorward angular momentum

transport by Reynolds stresses and that the meridional circulation tends to oppose this transport. In many previous simulations, the poleward angular momentum transport by the meridional circulation extends to higher latitudes, tending to spin up the poles. Thus, the slow polar rotation in case M3 and its hydrodynamic predecessors, cases H and AB, seems to come about from a relatively weak meridional circulation at high latitudes (see also Brun & Toomre 2002). The absence of strong high-latitude circulation cells permits a more efficient extraction of angular momentum by the Reynolds stresses from the polar regions toward the equator, yielding the interesting differential rotation profile that is achieved. Since the Maxwell stresses also transport angular momentum toward the poles, the polar regions in case M3 are found to rotate slightly faster than in case H. However, the angular momentum transport by Maxwell stresses is distributed such that the global rotation retains the attribute of a monotonic decrease of Ω with latitude.

6. EVOLUTION OF MEAN MAGNETIC FIELDS

It is clear from the results presented (see, e.g., Figs. 4, 7, 8, and 10) that the magnetic field is dominated by the fluctuating or turbulent (nonaxisymmetric) component. However, the mean (axisymmetric) field components have particular significance with regard to solar dynamo theory; thus, it is instructive to explore their structure and evolution in detail. In particular, we wish to understand our simulation results in the context of solar observations although we are aware that we are still missing important "dynamo building blocks" (see § 1.1) such as magnetic pumping into a tachocline-like shear layer. Our results provide fundamental insight into the generation of mean magnetic fields by turbulent convection and as such can be used to evaluate and improve mean field dynamo models that do not explicitly consider the turbulent field and flow
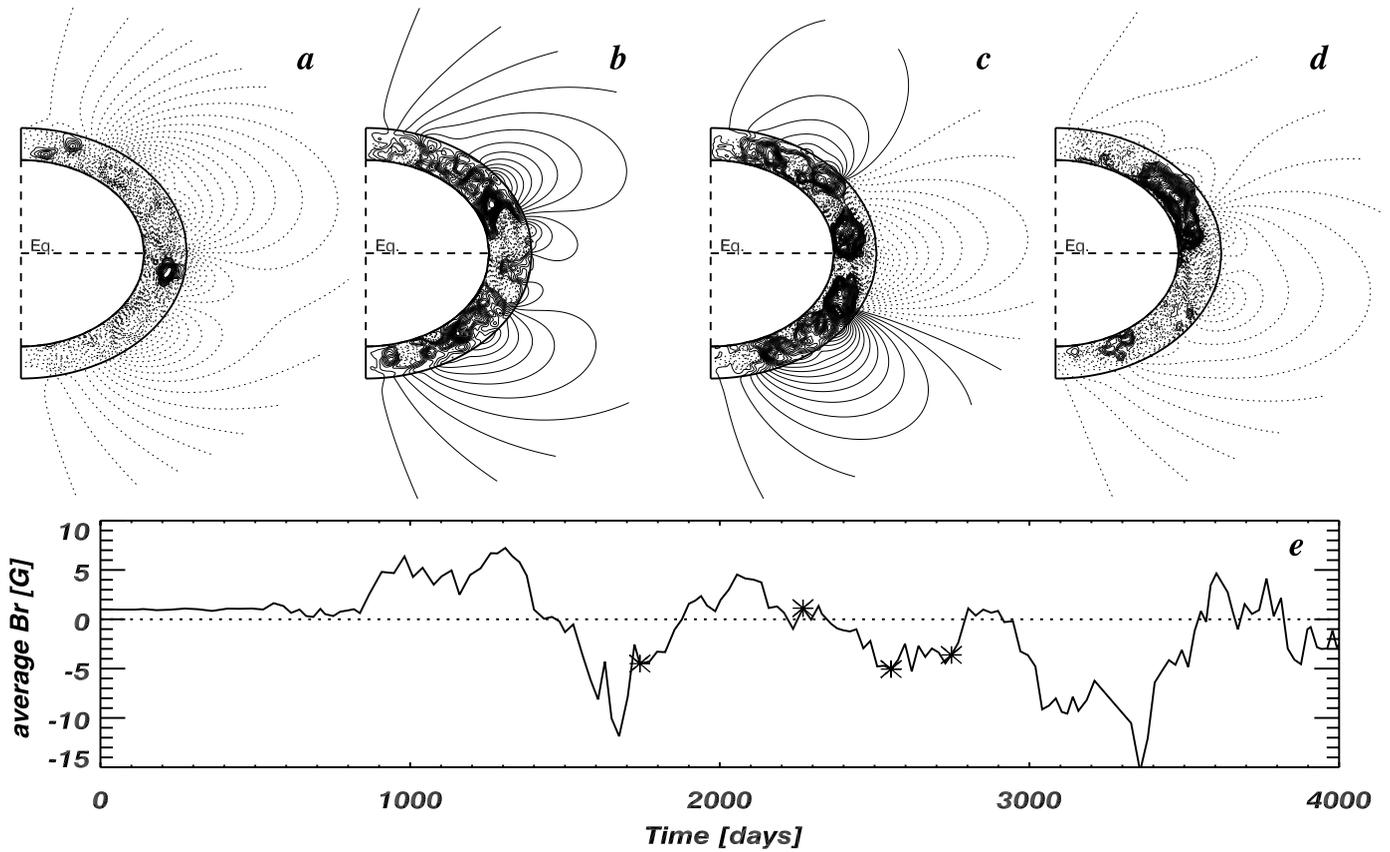
FIG. 11.—Temporal evolution of the mean poloidal field for case M3. (*a–d*) Structure of the field at four selected times after the magnetic energy has reached a statistically steady state. Solid contours denote positive polarity (clockwise orientation), and dotted contours denote negative polarity. (*e*) Mean radial field at the outer boundary averaged over the northern hemisphere, shown over the course of the entire simulation. The average polarity reverses after about 1750 days and several more times afterward on a timescale of about 500 days. However, the field generally exhibits a complex topology with both symmetric and antisymmetric components. The instants in time corresponding to the top panels are indicated in (*e*) with asterisks.

components (e.g., Krause & Rädler 1980; Ossendrijver 2003). In what follows, we define the mean poloidal field in terms of the longitudinally averaged radial and latitudinal components, $\langle B_p \rangle = \langle B_r \rangle \hat{e}_r + \langle B_\theta \rangle \hat{e}_\theta$, and the mean toroidal field in terms of the longitudinally averaged longitudinal component, $\langle B_t \rangle = \langle B_\phi \rangle \hat{e}_\phi$.

The generation of the mean toroidal field in our simulations is due to the shearing, stretching, and twisting of mean and fluctuating poloidal fields by differential rotation (the ω-effect) and helical convective motions (the α-effect). Likewise, mean poloidal fields are generated from fluctuating toroidal fields via the α-effect. The α-effect arises from correlations between turbulent flows and fields as expressed in the mean (longitudinally averaged) induction equation by the term $\Psi = \langle \nabla \times (v' \times B') \rangle$, where primes indicate that the axisymmetric component has been subtracted off and angular brackets indicate a longitudinal average (Moffatt 1978; Stix 2002; Brandenburg & Subramanian 2004). We find that the fluctuating fields in our simulations are much stronger than the mean fields, accounting for up to 98% of the total magnetic energy, and the scale and amplitude of their correlations are not small in any sense and therefore cannot be reliably parameterized in terms of the mean field. It appears that the generation of mean fields in our simulations is not due to the α-effect in the traditional sense, but rather to a more complex interplay between turbulent magnetic field and flow components. The chaotic nature of these turbulent components gives rise to intricate structure and aperiodic evolution in the mean fields.

6.1. *Poloidal Fields*

Figure 11 illustrates the structure and evolution of the mean poloidal field in case M3. Figures 11*a*–11*d* show four snapshots of the magnetic lines of force of $\langle B_p \rangle$ within the convective domain along with a potential extrapolation of the external field up to $2R_*$. The initial seed field was dipolar (i.e., antisymmetric with respect to the equator), but symmetric fields (i.e., quadrupolar configurations) are also realized in our simulations, as in Figure 11*c*. The evolution of the poloidal magnetic field from an antisymmetric to a symmetric profile with respect to the equator is made possible because of the nonlinear and asymmetric nature of the convection that amplifies the field through dynamo action. The continuous exchange between dipolar and quadrupolar topologies, as well as higher order multipoles, results in magnetic fields with intricate configurations and with no clear equatorial symmetry preferences. Within the convective shell the presence of strong magnetic field gradients and magnetic diffusion leads to continuous reconnection of the magnetic field lines.

The perpetual regeneration of magnetic flux by the convection can lead to a global reversal of the magnetic field polarity. Figure 11*e* shows the temporal evolution of the average polarity of the poloidal field in case M3, defined in terms of the radial magnetic field B_r averaged over the northern hemisphere of the outer boundary. This is a measure of the total magnetic flux that passes through the northern hemisphere at the outer surface of the shell, and since $\nabla \cdot B = 0$ outside as well as
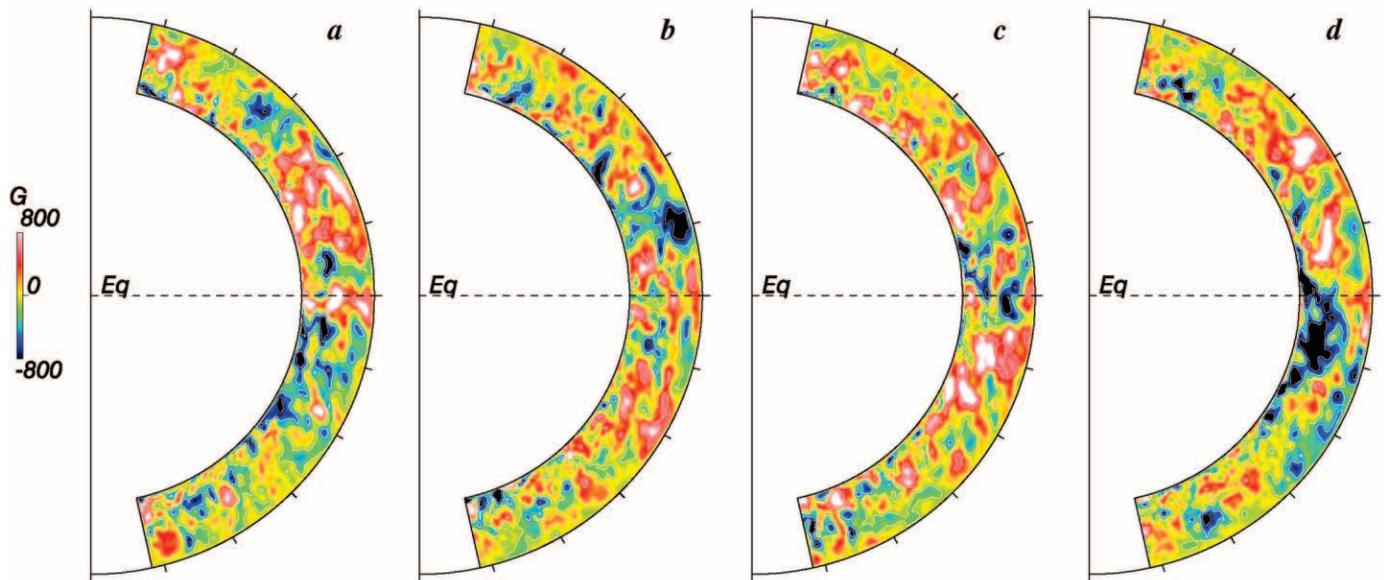
Fig. 12.—Evolution of the mean toroidal field for case M3, as a companion to Fig. 11. Red and blue tones denote eastward (prograde) and westward (retrograde) field, respectively, as indicated by the color table.

inside the domain, the same flux of opposite polarity must also pass through the southern hemisphere. A positive value indicates that the field is outward on average in the northern hemisphere, as in the dipolar initial conditions. By contrast, a negative value indicates that the average polarity is opposite to that imposed in the initial conditions.

The flat evolution over the first 800 days corresponds to the linear growth phase of the magnetic energy, where the field evolves slowly away from its imposed initial dipolar topology and north-south orientation. As the fields with negative polarity gain in strength, a complex competition between the two polarities, directly related to the turbulent nature of the dynamo, leads to a chaotic and irregular variation of the average polarity. Several field reversals do occur on a timescale of about 500 days, but there is little evidence for systematic cyclic behavior. This timescale is comparable to the 1.5 yr periods found by Gilman (1983) in some of his Boussinesq dynamo simulations. Glatzmaier (1985a, 1987) inferred longer reversal timescales ($\sim$10 yr) in his simulations that incorporated compressibility via the anelastic approximation as here and included convective penetration into an underlying stable region. Like Glatzmaier's, our simulations only cover about 10 yr so they would not capture longer term cyclic behavior if it were present. However, the chaotic short-term evolution suggests that longer term periodic behavior is unlikely for the configuration that we have adopted here.

Our high-resolution simulations confirm that the timescale for field reversal within the convective envelope itself is too short and that without a stable layer such as the solar tachocline such simulations are unlikely to reproduce the global-scale dynamo and 22 yr activity cycle observed in the Sun. There is no systematic latitudinal propagation of $\langle B_p \rangle$ over the 4000 days that we have been able to compute. Rather, the temporal evolution of $\langle B_p \rangle$ is quite complex and highly unpredictable, governed by advection and amplification by turbulent convective motions. Both Gilman and Glatzmaier found poleward propagation of $\langle B_p \rangle$. The main difference between their convective dynamo simulations and ours comes from the level of turbulence and nonaxisymmetry. In case M3, the axisymmetric

fields are weak and do not control the dynamical evolution of the flow and magnetic fields but seem, on the contrary, passive, which could in part explain their erratic evolution. The mean poloidal field is generated mainly by the coupling between fluctuating field and flow components, and the generation rate is not in general proportional to the strength of the mean field as is assumed in the classical α-effect.

6.2. Toroidal Fields

Figure 12 shows the mean toroidal magnetic field $\langle B_t \rangle$ for the same time snapshots as displayed in Figure 11. We can readily see that it possesses small-scale structure that varies substantially with time. Mixed polarities and intricate topologies are present throughout the simulation domain, with no evident symmetries with respect to the equator. Instantaneous snapshots or time averages reveal weak responses with varying symmetries, but these do not persist for any extended interval. Structures resembling thin tubes with circular cross sections are present, but they generally do not remain coherent long enough to rise and emerge through the surface as a result of magnetic buoyancy. No systematic latitudinal propagation of $\langle B_t \rangle$ is evident in this time sequence or in any that we have studied. This is in contrast with solar observations that reveal regular trends in the emergence of sunspots and related magnetic flux over the 22 yr activity cycle.

The mean toroidal field contains about 1.5% of the total magnetic energy, about a factor of 3 larger than the energy in the mean poloidal field. The production terms in the mean induction equation due to differential rotation (the ω-effect) and convective motions (the α-effect) are of the same order so our simulations may be loosely classified as α^2-ω dynamos.

In the Sun the ratio of mean toroidal to poloidal magnetic energy is at least 100, suggesting that the Sun may not be generating its mean toroidal field solely in the convective zone. Glatzmaier (1984, 1985a, 1985b, 1987) incorporated convective penetration into an underlying stable layer in his dynamo simulations and found that $\langle B_t \rangle$ was a significant fraction ($\sim$85%) of the total magnetic energy. This result suggests that strong axisymmetric toroidal fields are generated

mainly in the stable layer via the ω-effect and strengthens the current paradigm that convection in the solar envelope cannot amplify the mean toroidal field to observed levels without the presence of convective penetration into a stably stratified shear layer such as the solar tachocline. The convection zone continuously supplies disorganized magnetic fields over a wide range of spatial scales to the tachocline, where they are then amplified and organized into extended toroidal structures.

7. FURTHER ASPECTS OF FIELD GENERATION

7.1. *Helicity in Flows and Fields*

It has long been realized that helicity can play an essential role in hydromagnetic dynamo action, particularly in the solar context. Parker's (1955) classical paradigm for the solar dynamo relies on twisting motions in order to generate poloidal field from toroidal field and thus drive the solar activity cycle. Mean field analyses of homogeneous MHD turbulence based on the assumption of scale separation yield an explicit expression for the regeneration rate of the magnetic field (the α-effect) that is directly proportional to the kinetic helicity of the flow, defined as the dot product of velocity and vorticity: $H_k = \boldsymbol{\omega} \cdot \boldsymbol{v}$ (e.g., Moffatt 1978; Krause & Rädler 1980).

The kinetic helicity provides a measure of how much twist is present in the velocity field. Magnetic twist (and writhe; see Moffatt & Ricca 1992) is often measured by the magnetic helicity, defined as the dot product of the magnetic field and the vector potential: $H_m = \boldsymbol{A} \cdot \boldsymbol{B}$. This quantity has particular theoretical significance because it is conserved in ideal (dissipationless) MHD (Biskamp 1993). However, magnetic helicity is very difficult to measure reliably on the Sun. From an observational standpoint, a more practical measure of magnetic twist is the current helicity, defined as the scalar product of the magnetic field and current density: $H_c = \boldsymbol{J} \cdot \boldsymbol{B}$.

Measurements of the radial component of the current helicity in the solar photosphere have revealed a weak latitudinal dependence, tending toward negative values in the northern hemisphere and positive values in the southern hemisphere (Pevtsov et al. 1994, 1995). Helicity indicators in the chromosphere and corona reveal similar hemisphere rules for a variety of structures; the pattern is particularly strong for relatively large scale features such as X-ray sigmoids (Zirker et al. 1997; Pevtsov 2002; Pevtsov et al. 2003). It has been suggested that the expulsion of this magnetic helicity by coronal mass ejections may play a crucial role in altering the global topology of the coronal field during polarity reversals (Low 2001; Low & Zhang 2004).

Figure 13 illustrates the kinetic and current helicity in simulation M3. The kinetic helicity shows a clear variation with latitude. Its amplitude peaks in the upper convection zone where it is negative in the northern hemisphere and positive in the southern hemisphere, reflecting the influence of rotation and density stratification; expanding upflows spin down and contracting downflows spin up, tending to conserve their angular momentum (e.g., Miesch et al. 2000). In the lower convection zone the helicity reverses as downflows encounter the lower boundary and diverge, inducing anticyclonic vorticity. The horizontal view in Figure 13 indicates that much of the kinetic helicity is confined to downflow lanes, reflecting their vortical nature.

The current helicity also tends to peak in downflow lanes, but its latitudinal variation is much less systematic than the kinetic helicity. Current helicity of both signs appears in each hemisphere, often juxtaposed in the same downflow lane. The

amplitude of the magnetic helicity peaks in the lower convection zone where there is a weak pattern of positive and negative values in the northern and southern hemisphere, respectively.

These simulation results suggest that the helicity patterns observed in the solar atmosphere may not be produced by turbulent convection in the envelope. Rather, they may originate in the tachocline where flux tubes are formed and subsequently rise to the surface owing to magnetic buoyancy to form active regions. Alternatively, the patterns may arise from the action of Coriolis forces as flux tubes rise through the convection zone or from footpoint motions after they have emerged (e.g., Pevtsov 2002; Fan 2004).

7.2. *Spectral Distributions*

The convection patterns shown in Figure 4 suggest that the magnetic field possesses relatively more small-scale structure than the velocity field. This is verified by the energy spectra shown in Figure 14. The slope of the magnetic energy spectrum is much shallower than the kinetic energy spectrum and generally peaks at higher wavenumbers. Thus, the magnetic energy equals or exceeds the kinetic energy at small scales, even though the ratio of total magnetic to kinetic energy remains small. Throughout most of the convection zone, the magnetic energy spectrum peaks near $\ell \sim 30$, compared with $\ell \sim 12-15$ for the kinetic energy. Near the top of the domain the kinetic energy spectrum peaks at somewhat larger scales $\ell \sim 10$, whereas the magnetic energy spectrum remains relatively flat in the range $\ell = 1-20$.

At degrees $\ell \gtrsim 30$, the spectra suggest some power-law behavior, but it extends for less than a decade in degree so these simulations do not possess an extended inertial range. The slope of the kinetic energy spectrum is substantially steeper than that expected for homogeneous, isotropic, incompressible turbulence, with ($\ell^{-3/2}$) or without ($\ell^{-5/3}$) magnetic fields (e.g., Biskamp 1993). Estimates based on curve fits to the kinetic energy spectrum yield slopes steeper than ℓ^{-3}. The magnetic energy spectra are shallower but still fall off faster than predicted for homogeneous, isotropic, incompressible MHD turbulence ($\ell^{-3/2}$).

7.3. *Probability Density Functions*

The pdf's can generally provide more information about the structure and dynamics of a flow than spectral analyses alone. Indeed, in a homogeneous flow, the energy spectra are simply related to the first moment of the corresponding two-point pdf. We here consider the one-point pdf of the velocity and magnetic field variables as given by the histogram of values at all grid points, corrected for the grid convergence at the poles. Results are shown in Figure 15.

Idealized isotropic, homogeneous turbulence has Gaussian velocity pdf's, but departures from Gaussian statistics are known to be present in real-world turbulent flows. Velocity differences and derivatives in particular generally have non-Gaussian pdf's that are often characterized by stretched exponentials $\exp(-\beta)$ with $0.5 \leq \beta \leq 2$ (e.g., She et al. 1988; Castaing et al. 1990; Vincent & Meneguzzi 1991; Kailasnath et al. 1992; Pumir 1996). The tails of the distributions are often nearly exponential ($\beta \approx 1$) but can be even flatter, particularly in the viscous dissipation range. A flat slope ($\beta < 2$) indicates an excess of extreme (high amplitude) events relative to a Gaussian distribution, thus reflecting spatial intermittency in the flow that may be associated with coherent
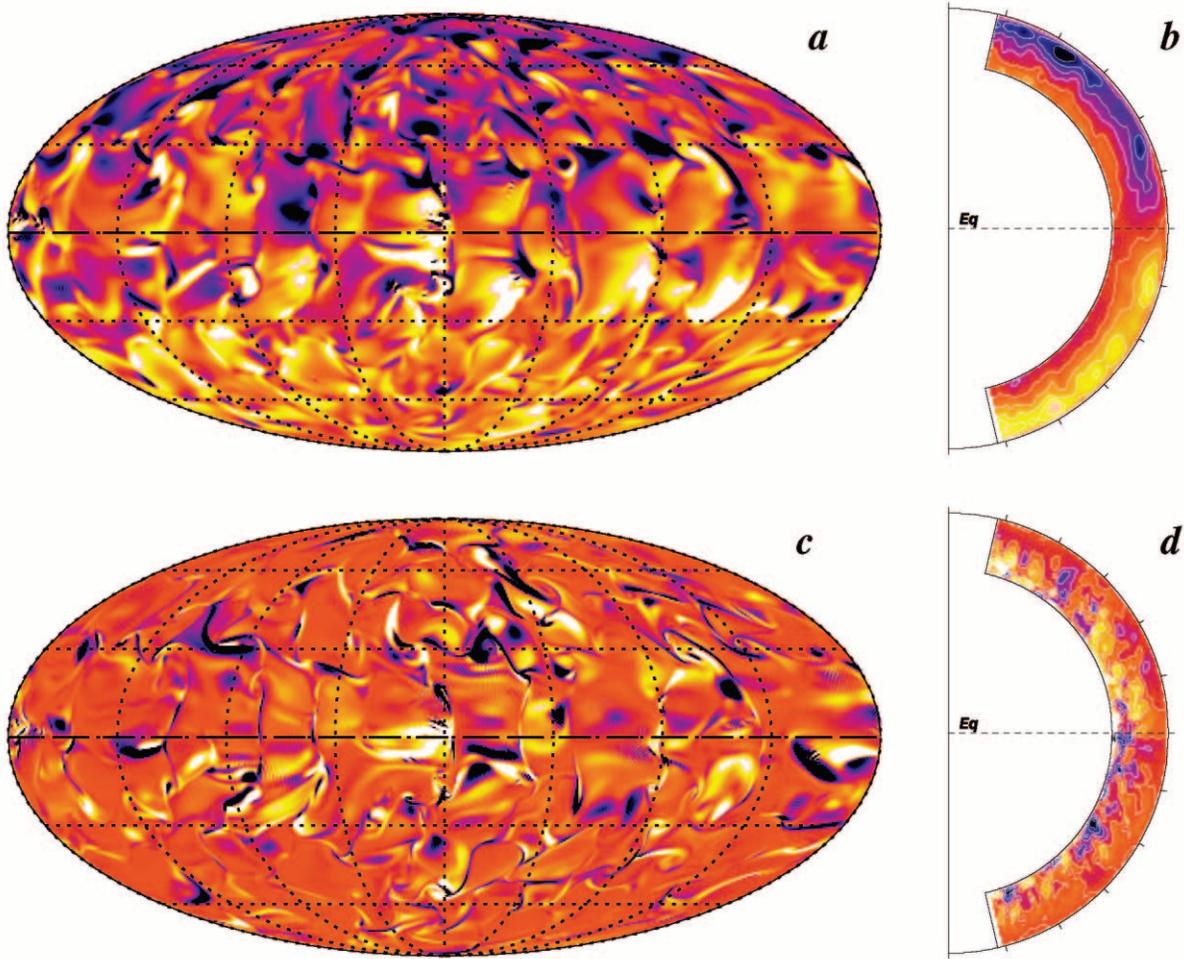
Fig. 13.—(a, b) Kinetic helicity H_k and (c, d) current helicity H_c in case M3. Panels (a) and (c) show global views at the same time and horizontal level (near the top of the layer) as in Fig. 4, and panels (b) and (d) display meridional profiles averaged over longitude and time. Bright tones denote positive values and dark tones negative values (the color table is as in Fig. 1).

structures (e.g., Vincent & Meneguzzi 1991; Lamballais et al. 1997).

Another way to quantify the asymmetry and intermittency of selected flow and field variables is through moments of the pdf, in particular the skewness $\mathcal{S}$ and kurtosis $\mathcal{K}$, defined as

$$\mathcal{S} = \frac{\int (x - \mu)^3 f(x)\,dx}{\sigma^3 \int f(x)\,dx}, \quad \mathcal{K} = \frac{\int (x - \mu)^4 f(x)\,dx}{\sigma^4 \int f(x)\,dx}, \quad (27)$$

where $f(x)$ is the pdf, x is the abscissa, μ is the mode of the distribution, and σ is the standard deviation:

$$\sigma = \left[\frac{\int (x - \mu)^2 f(x)\,dx}{\int f(x)\,dx} \right]^{1/2}. \quad (28)$$

Gaussian pdf's are characterized by $\mathcal{S} = 0$ and $\mathcal{K} = 3$ and exponential pdf's ($\beta = 1$) by $\mathcal{S} = 0$ and $\mathcal{K} = 6$. A large value for $\mathcal{S}$ indicates asymmetry in the pdf, whereas a large value of $\mathcal{K}$ indicates a high degree of spatial intermittency.

The pdf's for turbulent, compressible, MHD convection in Cartesian geometries have been reported by Brandenburg et al. (1996). They found that the velocity pdf's were generally asymmetric and intermittent, with $\mathcal{K} \simeq 4$–5 for the horizontal components and $\mathcal{K} \simeq 8$ for the vertical component. The

vorticity, magnetic field, and current density were more symmetric but also much more intermittent, possessing kurtosis values of $\mathcal{K} \simeq 20$ for $\boldsymbol{B}$ and ω and $\mathcal{K} \simeq 30$ for $\boldsymbol{J}$.

The pdf's in case M3 (Fig. 15) are qualitatively similar to those found by Brandenburg et al. (1996). The radial velocity has nearly exponential tails ($\mathcal{K} = 4.6$) and a negative skewness ($\mathcal{S} = -0.98$); the fastest downflows are more than 150 m s^{-1} compared to about 120 m s^{-1} for upflows. The zonal velocity, v_ϕ, is more Gaussian ($\mathcal{K} = 2.4$) but still asymmetric ($\mathcal{S} = 0.45$), reflecting the influence of the differential rotation. The enstrophy also appears nearly exponential but with two distinct slopes, flattening out for the highest amplitude events. This implies a very high degree of intermittency ($\mathcal{K} = 270$). The radial and toroidal magnetic fields are more intermittent than the velocity field ($\mathcal{K} = 79, 11$) and appear to be more symmetric, although several outlier points in the extreme tails of the B_r pdf give rise to a relatively large skewness, $\mathcal{S} = -1.3$ ($\mathcal{S} = 0.18$ for the B_ϕ pdf). Maximum field strengths reach about 5000 G for the toroidal field and somewhat less (2000 G) for the radial field. The relatively intermittent spatial structure of the magnetic field is also apparent in the pdf of J^2, which possesses an even higher kurtosis ($\mathcal{K} = 440$) than the enstrophy. Note that the kurtosis values quoted here for the enstrophy and current density pdf's are much higher than those reported by Brandenburg et al. (1996) primarily because they considered
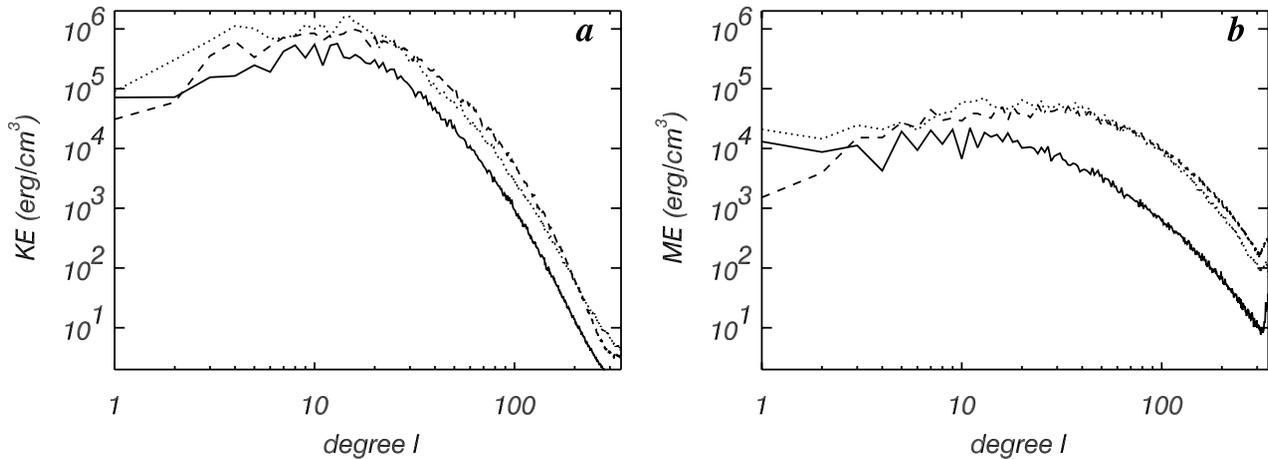
Fig. 14.—Time-averaged (*a*) kinetic and (*b*) magnetic energy spectra shown vs. spherical harmonic degree ℓ (including all azimuthal wavenumbers *m* but *m* = 0), for case M3 near the top, middle, and bottom of the convection zone (*solid, dashed, and dotted lines, respectively*).

the linear vector fields ω and $\boldsymbol{J}$ whereas we have considered the nonlinear scalar products ω^2 and J^2.

8. SUMMARY

In this paper we report the highest resolution three-dimensional simulations achieved to date of hydromagnetic dynamo action by global-scale turbulent convection and differential rotation in the solar envelope. Building on our own previous hydrodynamic simulations and the pioneering dynamo models of Gilman (1983) and Glatzmaier (1984), we have investigated the generation and maintenance of mean and fluctuating magnetic fields in the solar convection zone, focusing on their structure, evolution, and dynamical influence on the flow field through Lorentz forces. Our simulations are not intended to provide a comprehensive model of the solar dynamo; they do not address important ingredients such as toroidal field generation and storage in the tachocline or flux emergence through the photosphere. Still, they provide essential insight into a crucial element of the global dynamo process, namely, the generation of and coupling between poloidal and toroidal magnetic fields in the convection zone, which is often described in terms of an α-effect and ω-effect.

The numerical experiments we have performed involve the addition of a small seed magnetic field to an existing hydrodynamic simulation. For the parameter regimes considered here, we find that sustained dynamo action occurs when the magnetic Reynolds number Re_m exceeds about 300. If this is the case, then the seed magnetic field grows exponentially and subsequently saturates, reaching a statistically steady state as Lorentz forces begin to feed back on the flow field. Throughout most of this paper we focus on our simulation with the lowest magnetic diffusivity, case M3 ($\mathrm{Re}_m = 486$), in which the steady state magnetic energy is about 7% of the total kinetic energy contained in the convection and differential rotation. At this level of magnetism, Lorentz forces are not strong enough to dramatically change the appearance of the flow; convective patterns in case M3 are similar to those in the nonmagnetic progenitor simulation, case H. Furthermore, the radial energy flux balance through the shell is essentially unaffected; the Poynting flux is negligible and the net convective and diffusive energy fluxes are nearly the same as in case H.

Although Lorentz forces have little effect on the appearance of the convection in case M3 relative to case H, they do have a

substantial influence on the structure and evolution of mean flows. Fluctuating magnetic fields transport angular momentum poleward via Maxwell stresses, decreasing the magnitude of the differential rotation. This leads to a decrease in the angular velocity contrast between the equator and latitudes of $60°$ from 34% in case H to 24% in case M3. Magnetic tension forces associated with the mean (axisymmetric) poloidal field also tend to suppress rotational shear, but this process is much less efficient than Maxwell stresses and plays a negligible role in the maintenance of the global rotation profile. Despite the inhibiting effects of Lorentz forces, case M3 is able to sustain a strong differential rotation comparable in amplitude and structure to the solar internal rotation inferred from helioseismology.

The meridional circulation in the simulations reported here is generally characterized by multiple cells in latitude and radius and large temporal variations over timescales of weeks and months. This spatial and temporal variation is not surprising, since the circulation arises from small differences in large forces that fluctuate substantially in space and time, including Reynolds stresses, Maxwell stresses, thermal (baroclinic) driving, and Coriolis forces operating on the differential rotation. Still, it is in sharp contrast to many solar dynamo models that assume that the meridional circulation is relatively smooth and steady, dominated by one or two large cells in each hemisphere (e.g., Wang & Sheeley 1991; Durney 1997; Dikpati & Charbonneau 1999). Doppler measurements of photospheric flows and local-domain helioseismic inversions typically reveal systematic circulation patterns in the surface layers of the Sun, with poleward flow of about 20 m s^{-1} at low latitudes and some time variation (e.g., Hathaway et al. 1996; Haber et al. 2000). Although these analyses lie outside our computational domain, the results are roughly consistent with our simulations: the meridional flows at low latitudes near the top of the shell are consistently poleward when averaged over several months, although these cells only extend up to about $30°$ in latitude (see Fig. 9). Somewhat deeper helioseismic probing (down to $\sim 0.98 R_*$), still in local domains, provides some evidence for large temporal fluctuations and multiple cells in radius (Haber et al. 2002), but little is currently known about circulation patterns below about $0.97 R_*$. Characterizing the nature of the meridional flow in the deep convection zone is thus an important future challenge for helioseismology.
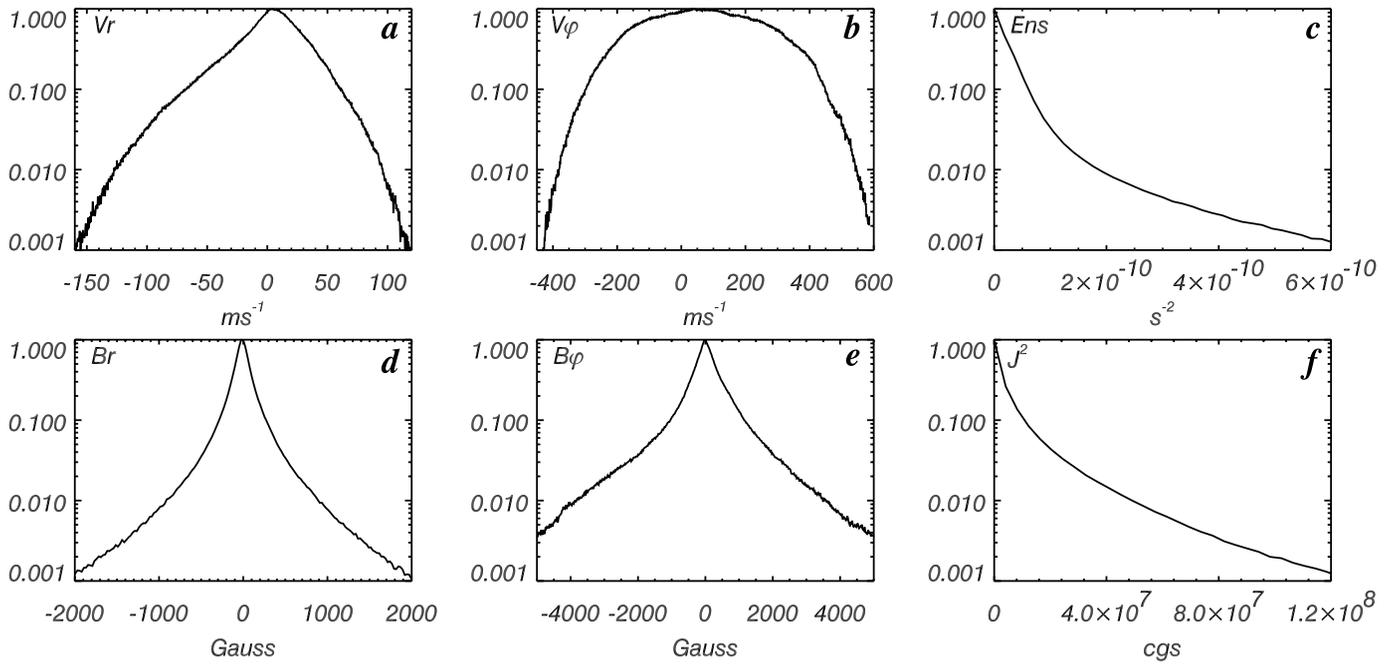
Fig. 15.—The pdf's of (*a*) the radial velocity v_r, (*b*) the zonal velocity v_ϕ, (*c*) the enstrophy ω^2, (*d*) the radial magnetic field B_r, (*e*) the toroidal magnetic field B_ϕ, and (*f*) the square of the current density J^2 in case M3. All pdf's are averaged over time and correspond to a horizontal level near the top of the shell.

About 98% of the magnetic energy in our simulations is contained in the fluctuating (nonaxisymmetric) field components that dominate the Lorentz forces and the induction equation. These components exhibit a complex spatial structure and rapid time evolution as they are amplified, advected, and distorted by convective motions. The distortion is particularly pronounced at midlatitudes, around 25°, where there is a change in the nature of the convective patterns from the north-south aligned downflow structures that dominate the equatorial regions to the more isotropic high-latitude network. The magnetic field possesses more small-scale structure and is significantly more intermittent than the velocity field, a result that is best demonstrated by considering the spectra and pdf's presented in § 7. The pdf's are in general non-Gaussian and asymmetric, in contrast to homogeneous, isotropic turbulence.

There is a noticeable difference in the topology of the radial and toroidal magnetic field components. Particularly near the top of the convection zone, the radial field B_r concentrates in downflow lanes where fields of opposite polarity are brought together by converging horizontal flows, thus promoting magnetic reconnection, and where magnetic structures are twisted and distorted by vorticity and shear. Both the kinetic helicity $\omega \cdot v$ and the current helicity $\boldsymbol{J} \cdot \boldsymbol{B}$ peak in these vortical downflow lanes. However, unlike the kinetic helicity, the current helicity does not exhibit a strong sign reversal in the northern and southern hemispheres; both signs are distributed across all latitudes, often in close proximity. A potential extrapolation of the radial field beyond the outer boundary of our domain reveals a complex web of magnetic loops, exhibiting both local and long-range connectivity across the surface.

Relative to the radial field, the toroidal field B_ϕ is organized into larger scale ribbons and sheets that are stretched out in longitude by the differential rotation and that are not in general confined to downflow lanes. Near the top of the convection zone, broad patches of like-signed toroidal field exist between the north-south aligned downflow lanes at low latitudes. These patches are typically confined to the surface layers, with a

relatively small radial extent. Although some structures resemble toroidal flux tubes, they are rapidly advected and distorted by convective motions and generally lose their identity before magnetic buoyancy forces would otherwise cause them to rise and emerge from the surface. Peak field strengths reach about 4000–5000 G for the toroidal field and about 2000 G for the radial field.

The mean poloidal and toroidal fields have much smaller amplitudes than the fluctuating fields in our simulations, but nevertheless they have particular significance for solar dynamo theory. Our simulations do not exhibit the organized structure, systematic propagation patterns, and periodic polarity reversals that are known to exist in the Sun. Rather, they possess a relatively complex spatial and temporal dependence that can be attributed to the highly nonlinear nature of the fluctuating velocity and magnetic field correlations through which they are principally maintained.

The energy in the mean toroidal field in case M3 is about a factor of 3 larger than that in the mean poloidal field. This asymmetry suggests that the differential rotation plays an important role in the generation of mean fields via the ω-effect, in addition to the contribution from convective motions that can be loosely regarded as a (nontraditional) α-effect. By contrast, the fluctuating poloidal and toroidal fields are comparable in amplitude, suggesting that the ω-effect plays a smaller role. However, the influence of differential rotation is still evident in the morphology of the fluctuating toroidal field (see Fig. 7*b*). The magnitude of the mean poloidal field near the surface in our simulations ($\sim$5–10 G; see Fig. 11) is comparable to the large-scale poloidal field at the surface of the Sun estimated from photospheric and coronal observations (e.g., Gibson et al. 1999). However, the peak strength of the mean toroidal field in our simulations ($\sim$800 G) is less than the field strength thought to exist in concentrated flux tubes in the solar interior where the estimated field strength ranges from 10^4–10^5 G near the base of the convection zone to $\sim$$10^3$ G near the surface (e.g., Fisher et al. 2000). The relatively weak toroidal fields in our simulations

can likely be attributed to the absence of a tachocline where toroidal flux can be efficiently stored and amplified by strong rotational shear.

The tachocline is an essential ingredient of the solar dynamo that is missing from the models reported here. It likely plays a central role in many aspects of the solar activity cycle, including the structure, strength, and emergence latitudes of sunspots and active regions as reflected, for example, by the well-known ''butterfly diagram.'' The large differential rotation and stable stratification in the lower portion of the tachocline promote the generation and storage of strong toroidal fields, which are thought to account for much of the magnetic activity observed in the solar atmosphere. Coupling between the convection zone and the radiative interior may also help to regularize the structure and evolution of the mean poloidal field, producing dipole configurations and cyclic reversals. We are now working to improve our dynamo simulations by incorporating convective penetration into an underlying stable region and a layer of rotational shear similar in nature to the solar tachocline. Results from these models will be published in forthcoming papers.

APPENDIX

MODEL EQUATIONS

The anelastic equations (1)–(7) (§ 2.1) define our physical model. Here we express these equations as they are solved by our numerical algorithm, making use of the velocity and magnetic field decomposition in equations (8) and (9). Diagnostic equations for the stream functions and potentials W, Z, A, and C are obtained by considering the vertical component of the momentum and induction equations and the vertical component of their curl. A Poisson equation for pressure can then be derived by taking the divergence of the momentum equation. However, the additional radial derivative this would require can compromise the accuracy of the solution, particularly when applied to the nonlinear advection terms. Since horizontal derivatives are more accurate than vertical derivatives, we choose to only take the horizontal divergence of the momentum equations rather than the full divergence. This results in a diagnostic equation for the horizontal divergence of the velocity field, which involves $\partial W / \partial r$ and the horizontal Laplacian of the pressure perturbation P. The system also includes the energy equation expressed in terms of the specific entropy perturbation S. A spherical harmonic transformation is applied to the governing equations before they are discretized in time so the time stepping occurs in spectral space: (ℓ, m, r). After some manipulation, the governing equations for the spherical harmonic coefficients of the state variables can be expressed as follows:

$$\frac{\ell(\ell+1)}{r^2}\frac{\partial W_{\ell m}}{\partial t} = \mathcal{L}^W + \mathcal{N}^W, \tag{A1}$$

$$-\frac{\ell(\ell+1)}{r^2}\frac{\partial}{\partial t}\left(\frac{\partial W_{\ell m}}{\partial r}\right) = \mathcal{L}^P + \mathcal{N}^P, \tag{A2}$$

$$\frac{\ell(\ell+1)}{r^2}\frac{\partial Z_{\ell m}}{\partial t} = \mathcal{L}^Z + \mathcal{N}^Z, \tag{A3}$$

$$\frac{\partial S_{\ell m}}{\partial t} = \mathcal{L}^S + \mathcal{N}^S, \tag{A4}$$

$$\frac{\ell(\ell+1)}{r^2}\frac{\partial A_{\ell m}}{\partial t} = \mathcal{L}^A + \mathcal{N}^A, \tag{A5}$$

$$\frac{\ell(\ell+1)}{r^2}\frac{\partial C_{\ell m}}{\partial t} = \mathcal{L}^C + \mathcal{N}^C. \tag{A6}$$

In these expressions, the $\mathcal{L}$ denote the linear diffusion, pressure gradient, buoyancy, and volume heating terms that are implemented using a semi-implicit, Crank-Nicholson time-stepping method:

$$\mathcal{L}^W = -\frac{\partial P_{\ell m}}{\partial r} - g\rho_{\ell m} + \nu\left[\frac{\ell(\ell+1)}{r^2}\right]\left\{\frac{\partial^2 W_{\ell m}}{\partial r^2} + \left(2\frac{d\ln\nu}{dr} - \frac{1}{3}\frac{d\ln\bar\rho}{dr}\right)\frac{\partial W_{\ell m}}{\partial r}\right.$$
$$\left. -\left[\frac{4}{3}\left(\frac{d\ln\nu}{dr}\frac{d\ln\bar\rho}{dr} + \frac{d^2\ln\bar\rho}{dr^2} + \frac{1}{r}\frac{d\ln\bar\rho}{dr} + \frac{3}{r}\frac{d\ln\nu}{dr}\right) + \frac{\ell(\ell+1)}{r^2}\right]W_{\ell m}\right\},$$

$$\mathcal{L}^P = \left[\frac{\ell(\ell+1)}{r^2}\right]P_{lm} - \nu\left[\frac{\ell(\ell+1)}{r^2}\right]\left\{\frac{\partial^3 W_{\ell m}}{\partial r^3} + \left(\frac{d\ln\nu}{dr} - \frac{d\ln\bar\rho}{dr}\right)\frac{\partial^2 W_{\ell m}}{\partial r^2}\right.$$

$$\left. - \left[\frac{2}{r}\frac{d\ln\bar\rho}{dr} + \frac{d^2\ln\bar\rho}{dr^2} + \frac{2}{r}\frac{d\ln\nu}{dr} + \frac{d\ln\nu}{dr}\frac{d\ln\bar\rho}{dr} + \frac{\ell(\ell+1)}{r^2}\right]\frac{\partial W_{\ell m}}{\partial r} - \left(\frac{d\ln\nu}{dr} + \frac{2}{r} + \frac{2}{3}\frac{d\ln\bar\rho}{dr}\right)\frac{\ell(\ell+1)}{r^2}W_{\ell m}\right\},$$

$$\mathcal{L}^Z = \nu\left[\frac{\ell(\ell+1)}{r^2}\right]\left\{\frac{\partial^2 Z_{\ell m}}{\partial r^2} + \left(\frac{d\ln\nu}{dr} - \frac{d\ln\bar\rho}{dr}\right)\frac{\partial Z_{\ell m}}{\partial r} - \left[\frac{2}{r}\frac{d\ln\nu}{dr} + \frac{d\ln\bar\rho}{dr}\frac{d\ln\nu}{dr} + \frac{d^2\ln\bar\rho}{dr^2} + \frac{2}{r}\frac{d\ln\bar\rho}{dr} - \frac{\ell(\ell+1)}{r^2}\right]Z_{\ell m}\right\},$$

$$\mathcal{L}^S = -\frac{\ell(\ell+1)}{r^2}\frac{d\bar S}{dr}W_{\ell m} + \frac{\kappa_r C_P}{\bar T}\left\{\frac{\partial^2}{\partial r^2} + \left[\frac{d}{dr}\ln(r^2\kappa_r\bar\rho)\right]\frac{\partial}{\partial r}\right\}(T_{\ell m} + \bar T) - \frac{\kappa_r C_P}{\bar T}\frac{\ell(\ell+1)}{r^2}T_{\ell m}$$

$$+ \kappa\left\{\frac{\partial^2}{\partial r^2} + \left[\frac{d}{dr}\ln(r^2\kappa\bar\rho\bar T)\right]\frac{\partial}{\partial r}\right\}(S_{\ell m} + \bar S) - \kappa\frac{\ell(\ell+1)}{r^2}S_{\ell m},$$

$$\mathcal{L}^A = \eta\left[\frac{\ell(\ell+1)}{r^2}\right]\left[\frac{\partial^2 A_{\ell m}}{\partial r^2} + \frac{d\ln\eta}{dr}\frac{\partial A_{\ell m}}{\partial r} - \frac{\ell(\ell+1)}{r^2}A_{\ell m}\right],$$

and

$$\mathcal{L}^C = \eta\left[\frac{\ell(\ell+1)}{r^2}\right]\left[\frac{\partial^2 C_{\ell m}}{\partial r^2} - \frac{\ell(\ell+1)}{r^2}C_{\ell m}\right].$$

The perfect gas equation of state implies

$$\rho_{\ell m} = \bar\rho\left(\frac{1}{\gamma}\frac{P_{\ell m}}{\bar P} - \frac{S_{\ell m}}{c_p}\right) \tag{A7}$$

and

$$T_{\ell m} = \bar T\left(\frac{\gamma-1}{\gamma}\frac{P_{\ell m}}{\bar P} + \frac{S_{\ell m}}{c_p}\right). \tag{A8}$$

The $\mathcal{N}$ terms in equations (A1)–(A6) include nonlinear advection terms that are implemented using an explicit, two-level Adams-Bashforth time-stepping method. Although the Coriolis terms are formally linear, they are also included in the $\mathcal{N}$ terms because, unlike the other linear terms, the resulting coefficients depend on azimuthal wavenumber m, and they couple the vertical vorticity equation to the vertical momentum and horizontal divergence equations. This would greatly complicate the matrix solution involved in the Crank-Nicholson method. Thus, the $\mathcal{N}$ terms in the momentum equations include Coriolis terms, which can be written in spherical harmonic space as

$$\mathcal{N}^W = \mathcal{A}_{\ell m}^W + \tau + \frac{2\Omega_0}{r}\left[\imath m\frac{\partial W_{\ell m}}{\partial r} - (\ell-1)c_\ell^m Z_{\ell-1}^m + (\ell+2)c_{\ell+1}^m Z_{\ell+1}^m\right],$$

$$\mathcal{N}^P = \mathcal{A}_{\ell m}^P + \frac{2\Omega_0}{r^2}\left\{-\imath m\left[\frac{\partial W_{\ell m}}{\partial r} + \frac{\ell(\ell+1)}{r}W_{\ell m}\right] + (\ell^2-1)c_\ell^m Z_{\ell-1}^m + \ell(\ell+2)c_{\ell+1}^m Z_{\ell+1}^m\right\},$$

and

$$\mathcal{N}^Z = \mathcal{A}_{\ell m}^Z + \frac{2\Omega_0}{r^2}\left[-\frac{\ell(\ell^2-1)}{r}c_\ell^m W_{\ell-1}^m + \frac{\ell(\ell+1)(\ell+2)}{r}c_{\ell+1}^m W_{\ell+1}^m + (\ell^2-1)c_\ell^m\frac{\partial W_{\ell-1}^m}{\partial r} + \ell(\ell+2)c_{\ell+1}^m\frac{\partial W_{\ell+1}^m}{\partial r} + \imath m Z_{\ell m}\right].$$

The τ appearing in $\mathcal{N}^W$ is the departure of the reference state from hydrostatic equilibrium (Clune et al. 1999). The $\mathcal{A}_{\ell m}^i$ in these equations represent the spherical harmonic coefficients of the nonlinear velocity advection terms and Lorentz forces. If we define their corresponding configuration space representation as

$$\mathcal{A}^i(r,\ \theta,\ \phi,\ t) = \sum_{\ell,m}\mathcal{A}_{\ell m}^i(r,\ t)Y_{\ell m}(\theta,\ \phi) \qquad (i = W,\ P,\ Z), \tag{A9}$$

then

$$\mathcal{A}^W = -\bar{\rho}\left(v_r\frac{\partial v_r}{\partial r} + \frac{v_\theta}{r}\frac{\partial v_r}{\partial \theta} + \frac{v_\phi}{r\sin\theta}\frac{\partial v_r}{\partial \phi} - \frac{v_\theta^2 + v_\phi^2}{r}\right) + J_\theta B_\phi - J_\phi B_\theta, \tag{A10}$$

$$\mathcal{A}^P = \frac{1}{r\sin\theta}\left[\frac{\partial}{\partial\theta}(\sin\theta\mathcal{A}_\theta) + \frac{\partial\mathcal{A}_\phi}{\partial\phi}\right], \tag{A11}$$

and

$$A^Z = \frac{1}{r\sin\theta}\left[\frac{\partial}{\partial\theta}(\sin\theta\mathcal{A}_\phi) - \frac{\partial\mathcal{A}_\theta}{\partial\phi}\right], \tag{A12}$$

where

$$\mathcal{A}_\theta = -\bar{\rho}\left(v_r\frac{\partial v_\theta}{\partial r} + \frac{v_\theta}{r}\frac{\partial v_\theta}{\partial \theta} + \frac{v_\phi}{r\sin\theta}\frac{\partial v_\theta}{\partial \phi} + \frac{v_r v_\theta}{r} - \frac{\cos\theta}{r\sin\theta}v_\phi^2\right) + J_\phi B_r - J_r B_\phi, \tag{A13}$$

$$\mathcal{A}_\phi = -\bar{\rho}\left(v_r\frac{\partial v_\phi}{\partial r} + \frac{v_\theta}{r}\frac{\partial v_\phi}{\partial \theta} + \frac{v_\phi}{r\sin\theta}\frac{\partial v_\phi}{\partial \phi} + \frac{v_r v_\phi}{r} + \frac{\cos\theta}{r\sin\theta}v_\theta v_\phi\right) + J_r B_\theta - J_\theta B_r, \tag{A14}$$

and $\boldsymbol{J} = \nabla \times \boldsymbol{B}/(4\pi)$. The dimensional current density is given by $\boldsymbol{j} = c\boldsymbol{J}$.

Likewise, the remaining $\mathcal{N}$ terms represent the spherical harmonic coefficients corresponding to the nonlinear terms in the energy and induction equations:

$$\mathcal{A}^i(r,\ \theta,\ \phi,\ t) = \sum_{\ell,m}\mathcal{N}^i(\ell,\ m,\ r,\ t)Y_{\ell m}(\theta,\ \phi) \qquad (i = S,\ A,\ C), \tag{A15}$$

where

$$\mathcal{A}^S = v_r\frac{\partial s}{\partial r} + \frac{v_\theta}{r}\frac{\partial s}{\partial \theta} + \frac{v_\phi}{r\sin\theta}\frac{\partial S}{\partial \phi} + \frac{2\nu}{\bar{T}}\left[e_{ij}e_{ij} - \frac{1}{3}\left(v_r\frac{d\ln\bar{\rho}}{dr}\right)^2\right] + \frac{4\pi\eta}{c^2\bar{\rho}\bar{T}}j^2 + \frac{\epsilon}{\bar{T}}, \tag{A16}$$

$$\mathcal{A}^A = -\frac{1}{r^2\sin\theta}\frac{\partial}{\partial\theta}\left(\sin\theta\frac{\partial\mathcal{E}_r}{\partial\theta}\right) - \frac{1}{r^2\sin^2\theta}\frac{\partial^2\mathcal{E}_r}{\partial\phi^2} + \frac{1}{r^2}\frac{\partial}{\partial r}\left\{\frac{r}{\sin\theta}\left[\frac{\partial}{\partial\theta}(\sin\theta\mathcal{E}_\theta) + \frac{\partial\mathcal{E}_\phi}{\partial\phi}\right]\right\}, \tag{A17}$$

$$\mathcal{A}^C = \frac{1}{r\sin\theta}\left[\frac{\partial}{\partial\theta}(\sin\theta\mathcal{E}_\phi) - \frac{\partial\mathcal{E}_\theta}{\partial\phi}\right], \tag{A18}$$

and $\mathcal{E} = \boldsymbol{v} \times \boldsymbol{B}$.

The boundary conditions discussed in § 2.1, expressed here in spectral space, require that the boundaries be impenetrable,

$$W_{\ell m}(r_{\text{bot}},\ t) = W_{\ell m}(r_{\text{top}},\ t) = 0, \tag{A19}$$

and stress-free,

$$\frac{\partial^2 W_{\ell m}}{\partial r^2}(r,\ t) - \left(\frac{2}{r} + \frac{d\ln\bar{\rho}}{dr}\right)\frac{\partial W_{\ell m}}{\partial r}(r,\ t) = 0 \qquad (r = r_{\text{bot}},\ r_{\text{top}}), \tag{A20}$$

$$\frac{\partial Z_{\ell m}}{\partial r}(r,\ t) - \left(\frac{2}{r} + \frac{d\ln\bar{\rho}}{dr}\right)Z_{\ell m}(r,\ t) = 0 \qquad (r = r_{\text{bot}},\ r_{\text{top}}). \tag{A21}$$

We also fix the entropy gradient at the top and bottom boundaries at the value defined by the initial reference state by requiring the perturbation entropy gradient to vanish:

$$\frac{\partial S_{\ell m}}{\partial r}(r_{\text{bot}},\ t) = \frac{\partial S_{\ell m}}{\partial r}(r_{\text{top}},\ t) = 0. \tag{A22}$$

The magnetic boundary conditions are chosen such that the interior field is continuous with an external potential field above and below the computational domain:

$$A_{\ell m}(r_{\text{bot}}, t) = A_{\ell m}(r_{\text{top}}, t) = 0, \tag{A23}$$

$$\frac{\partial C_{\ell m}}{\partial r}(r_{\text{top}}, t) + \frac{\ell}{r_{top}} C_{\ell m}(r_{\text{top}}, t) = 0, \qquad \frac{\partial C_{\ell m}}{\partial r}(r_{\text{bot}}, t) - \frac{\ell+1}{r_{bot}} C_{\ell m}(r_{\text{bot}}, t) = 0. \tag{A24}$$

For comparison purposes, we also did several simulations in which the magnetic field was required to be radial at the boundaries, corresponding to a highly permeable external medium (Jackson 1999):

$$\frac{\partial C_{\ell m}}{\partial r}(r, t) = 0, \qquad A_{\ell m}(r, t) = 0 \qquad (r = r_{\text{bot}}, r_{\text{top}}). \tag{A25}$$

Further details on the numerical algorithm are discussed in Clune et al. (1999).

REFERENCES

Babcock, H. W. 1961, ApJ, 133, 572
Beer, J., Tobias, S. M., & Weiss, N. O. 1998, Sol. Phys., 181, 237
Biskamp, D. 1993, Nonlinear Magnetohydrodynamics (Cambridge: Cambridge Univ. Press)
Brandenburg, A., Jennings, R. L., Nordlund, Å., Rieutord, M., Stein, R. F., & Tuominen, I. 1996, J. Fluid Mech., 306, 325
Brandenburg, A., & Subramanian, K. 2004, preprint (astro-ph/0405052)
Browning, M. K., Brun, A. S., & Toomre, J. 2004, ApJ, 601, 512
Brummell, N. H., Hurlburt, N. E., & Toomre, J. 1998, ApJ, 493, 955
Brun, A. S. 2004, Sol. Phys., 220, 333
Brun, A. S., Antia, H. M., Chitre, S. M., & Zahn, J.-P. 2002, A&A, 391, 725
Brun, A. S., & Toomre, J. 2002, ApJ, 570, 865
Busse, F. H. 1970, Phys. J. Fluid Mech., 44, 441
———. 2000a, Annu. Rev. Fluid Mech., 32, 383
———. 2000b, Phys. Fluids, 14, 1301
Busse, F. H., & Cuong, P. G. 1977, Geophys. Astrophys. Fluid Dyn., 8, 17
Castaing, B., Gagne, Y., & Hopfinger, E. J. 1990, Physica D, 46, 177
Cattaneo, F. 1999, ApJ, 515, L39
Cattaneo, F., Emonet, T., & Weiss, N. O. 2003, ApJ, 588, 1183
Cattaneo, F., & Hughes, D. W. 1996, Phys. Rev. E, 54, 4532
———. 2001, Astron. Geophys., 42 (3), 18
Charbonneau, P., & MacGregor, K. B. 1997, ApJ, 486, 502
Childress, S., & Gilbert A. D. 1995, Stretch, Twist, Fold: The Fast Dynamo (Berlin: Springer)
Christensen, U., Olson, P., & Glatzmaier, G. A. 1999, Geophys. J. Int., 138, 393
Clune, T. L., Elliott, J. R., Glatzmaier, G. A., Miesch, M. S., & Toomre, J. 1999, Parallel Comput., 25, 361
DeRosa, M. L., Gilman, P. A., & Toomre, J. 2002, ApJ, 581, 1356
Dikpati, M., & Charbonneau, P. 1999, ApJ, 518, 508
Durney, B. R. 1997, ApJ, 486, 1065
———. 1999, ApJ, 511, 945
Eddy, J. A., Gilman, P. A., & Trotter, D. E. 1976, Sol. Phys., 46, 3
Elliott, J. R., Miesch, M. S., & Toomre, J. 2000, ApJ, 533, 546
Fan, Y. 2004, Living Reviews in Solar Physics, http://solarphysics.livingreviews.org
Fisher, G. H., Fan Y., Longcope, D. W., Linton, M. G., & Pevtsov, A. A. 2000, Sol. Phys., 192, 119
Gibson, S. E., et al. 1999, ApJ, 520, 871
Gilman, P. A. 1983, ApJS, 53, 243
———. 2000, Sol. Phys., 192, 27
Gilman, P. A., & Miller, J. 1981, ApJS, 46, 211
Glatzmaier, G. A. 1984, J. Comput. Phys., 55, 461
———. 1985a, ApJ, 291, 300
———. 1985b, Geophys. Astrophys. Fluid Dyn., 31, 137
———. 1987, in The Internal Solar Angular Velocity, ed. B. R. Durney & S. Sofia (Dordrecht: Reidel), 263
Glatzmaier, G. A., & Gilman, P. 1982, ApJ, 256, 316
Gough, D. O., & Toomre, J. 1991, ARA&A, 29, 627
Grote, E., Busse, F. H., & Tilgner, A. 1999, Phys. Rev. E, 60, 5025
———. 2000, Phys. Earth Planet. Inter., 117, 259
Haber, D. A., Hindman, B. W., Toomre, J., Bogart, R. S., Larsen, R. M., & Hill, F. 2002, ApJ, 570, 855
Haber, D. A., Hindman, B. W., Toomre, J., Bogart, R. S., Thompson, M. J., & Hill, F. 2000, Sol. Phys., 192, 335
Harvey, J. W., et al. 1996, Science, 272, 1284
Hathaway, D. H., et al. 1996, Science, 272, 1306
Hindman, B. W., Gizon, L., Duvall, T. L., Jr., Haber, D. A. & Toomre, J. 2004, ApJ, 613, 1266

Howe, R., Christensen-Dalsgaard, J., Hill, F., Komm, R. W., Larsen, R. M., Schou, J., Thompson, M. J., & Toomre, J. 2000, ApJ, 533, L163
Ishihara, N., & Kida, S. 2002, J. Fluid Mech., 465, 1
Jackson, J. D. 1999, Classical Electrodynamics (3rd ed.; New York: Wiley)
Jacobs, J. A. 1987, Geomagnetism (London: Academic)
Kageyama, A., & Sato, T. 1997, Phys. Rev. E, 55, 4617
Kageyama, A., Watanabe, K., & Sato, T. 1993, Phys. Fluids B, 5, 2793
Kailasnath, P., Sreenivasan K. R., & Stolovitzky, G. 1992, Phys. Rev. Lett., 68, 2766
Kichatinov, L. L., & Rüdiger, G. 1995, A&A, 299, 446
Krause, F., & Rädler, K.-H. 1980, Mean-Field Magnetohydrodynamics and Dynamo Theory (1st ed.; Oxford: Pergamon)
Lamballais, E., Lesieur, M., & Métais, O. 1997, Phys. Rev. E, 56, 6761
Leighton, R. B. 1969, ApJ, 156, 1
Low, B. C. 2001, J. Geophys. Res., 106, 25141
Low, B. C., & Zhang, M. 2004, in Solar Variability and Its Effect on Climate (Geophys. Monogr. 141; Washington: AGU), 51
MacGregor, K. B., & Charbonneau, P. 1999, ApJ, 519, 911
Miesch, M. S., Elliott, J. R., Toomre, J., Clune, T. L., Glatzmaier, G. A., & Gilman, P. A. 2000, ApJ, 532, 593
Moffatt, H. K. 1978, Magnetic Field Generation in Electrically Conducting Fluids (Cambridge: Cambridge Univ. Press)
Moffatt, H. K., & Ricca, R. L. 1992, Proc. R. Soc. London A, 439, 411
Ossendrijver, M. 2003, A&A Rev., 11, 287
Parker, E. N. 1955, ApJ, 122, 293
———. 1989, Cosmical Magnetic Fields: Their Origin and Their Activity (Oxford: Clarendon)
———. 1993, ApJ, 408, 707
Pedlosky, J. 1987, Geophysical Fluid Dynamics (New York: Springer)
Pevtsov, A. A. 2002, in Multiwavelength Observations of Coronal Structures and Dynamics, ed. P. Martens & D. Cauffman (COSPAR Colloq. Ser. 13; Dordrecht: Pergamon), 125
Pevtsov, A. A., Balasubramaniam, K. S., & Rogers, J. W. 2003, ApJ, 595, 500
Pevtsov, A. A., Canfield, R. C., & Metcalf, T. R. 1994, ApJ, 425, L117
———. 1995, ApJ, 440, L109
Pumir, A. 1996, Phys. Fluids, 8, 3112
Roberts, P. H., & Glatzmaier, G. A. 2000, Rev. Mod. Phys., 72, 1081
Rüdiger, G., & Brandenburg, A. 1995, A&A, 296, 557
Scherrer, P. H., et al. 1995, Sol. Phys., 162, 129
Schou, J., et al. 1998, ApJ, 505, 390
She, Z.-S., Jackson, E., & Orszag, S. A. 1988, J. Sci. Comput., 3, 407
Spiegel, E. A., & Zahn, J.-P. 1992, A&A, 265, 106
Starr, V. P., & Gilman, P. A. 1966, Pure Appl. Geophys., 64, 145
Stein, R. F., & Nordlund, Å. 2000, Sol. Phys., 192, 91
Stix, M. 2002, The Sun: An Introduction (2nd ed.; Berlin: Springer)
Sun, Z.-P., & Schubert, G. 1995, Phys. Fluids, 7, 2686
Thompson, M. J., Christensen-Dalsgaard, J., Miesch, M. S., & Toomre, J. 2003, ARA&A, 41, 599
Thompson, M. J., et al. 1996, Science, 272, 1300
Tobias, S. M. 1996, A&A, 307, L21
Tobias, S. M., Brummell, N. H., Clune, T. L., & Toomre, J. 2001, ApJ, 549, 1183
Toomre, J. 2002, Science, 296, 64
Vincent, A., & Meneguzzi, M. 1991, J. Fluid Mech., 225, 1
Wang, Y. M., & Sheeley, N. R. 1991, ApJ, 375, 761
Weiss, N. O. 1994, in Lectures on Solar and Planetary Dynamos, ed. M. R. E. Proctor & A. D. Gilbert (Cambridge: Cambridge Univ. Press), 59
Zirker, J. B., Martin, S. F., Harvey, K., & Gaizauskas, V. 1997, Sol. Phys., 175, 27